Journal of Materials Chemistry A

ROYAL SOCIETY OF CHEMISTRY

PAPER

View Article Online
View Journal | View Issue

Cite this: J. Mater. Chem. A, 2025, 13, 6749

Regulating the electronic structure of $CoMoO_4$ *via* La doping for efficient and durable electrochemical water splitting reactions†

Bharathi Arumugam,[a] Erakulan E. Siddharthan,[b] Pandian Mannu,[c] Ranjit Thapa,[bd] Chung-Li Dong,[c] Arokia Anto Jeffery *[e] and Seong-Cheol Kim*[a]

Metal molybdates ($M'MoO_4$, M = Fe, Co, and Ni) are recognized as active catalysts for water-splitting reactions. However, their poor electronic conductivity and low intrinsic activity hamper overall water-splitting activity and durability, limiting their widespread applications. Herein, the influence of lanthanum doping on the electrocatalysis of $CoMoO_4$ toward overall water-splitting activity and durability in high-pH media was investigated. Varying La-dopant percentages in the $CoMoO_4$ lattice tuned the electrocatalytic activity, and optimal performance was achieved at 5% La_$CoMoO_4$ for hydrogen (η_{20} at 0.219 V_{RHE}) and oxygen evolution reactions (η_{20} at 0.272 V_{RHE}). Notably, La doping in $CoMoO_4$ mitigated significant MoO_4^{2-} leaching in the electrolyte, maintaining excellent structural integrity and demonstrating high durability for over 45 h in a two-electrode system, demanding a cell potential of only 1.68 V toward overall water splitting in 1 M KOH. Structural characterizations and *in situ* Raman studies established a dynamic surface reconstruction of active components toward the HER/OER. DFT analyses proved the modified electronic structure of $CoMoO_4$ through La doping, effectively optimizing adsorption energies of reactive hydrogen and oxygen intermediates and boosting the intrinsic activity of $CoMoO_4$ toward hydrogen and oxygen evolution reactions (HER/OER). This work depicts the prospect of rare-earth metal incorporation in non-noble metal-based electrocatalysts to design highly efficient and durable electrocatalysts for electrochemical applications.

Received 16th September 2024
Accepted 18th January 2025

DOI: 10.1039/d4ta06599a

rsc.li/materials-a

1. Introduction

In recent years, global pollution caused by the exploitation of and dependency on fossil fuels has instigated a transformation from fossil-based energy resources to green alternatives (solar, wind, and tidal energy) as sustainable renewable energy sources and is seriously being pursued to solve the ongoing energy crisis.[1,2] Electrocatalytic water splitting has emerged as a promising route to convert electric energy into a clean fuel such as hydrogen, which is used in industrial processes and fuel cells to generate electricity and powering vehicles. The electrolysis of water involves two half-reactions, namely, the hydrogen evolution reaction (HER) and oxygen evolution reaction (OER); however, the overall efficiency of the HER relies on the OER and depreciates gradually because of the complex and sluggish kinetics of the OER, requiring high overpotentials to endure multistep four-electron/proton transfer, thereby increasing high energy consumption.[3] Thus, developing a highly active bifunctional electrocatalyst is necessary to improve the overall kinetics of water oxidation. Noble metal catalysts, such as Pt and their alloys,[4] RuO_2 and/or IrO_2,[5] have been used as benchmark catalysts to accelerate the HER and OER owing to their high activity. Nevertheless, their poor stability, scarcity, and high costs limit practical commercialization.[6,7]

Earth-abundant transition-metal catalysts, especially those based on Fe, Co, Ni, Mn, Mo, and W, have garnered significant interest owing to their competent electrocatalytic activity and stability.[8] These catalysts include metal alloys,[9] carbides,[10] nitrides,[11] and metal chalcogenides[12–14] for the HER as well as metal phosphates,[15] metal sulfides,[16–18] metal oxides,[19,20] and metal hydroxides[21] for the OER, which have been widely explored to date. Notably, bimetallic oxides such as metal molybdates/tungstates ($MM'O_4$, M = Fe, Co, and Ni; M′ = Mo

[a]Department of Chemical Engineering, Yeungnam University, Gyeongsan, 38541, Korea. E-mail: sckim07@ynu.ac.kr
[b]Department of Physics, SRM University-AP, Amaravati, Andhra Pradesh, 522 240, India
[c]Department of Physics, Tamkang University, New Taipei City 25137, Taiwan
[d]Center for Computational and Integrative Sciences, SRM University-AP, Amaravati, Andhra Pradesh, 522 240, India
[e]Department of Bioengineering, Saveetha School of Engineering, Saveetha Institute of Medical and Technical Sciences (SIMATS), Chennai-602105, India. E-mail: jeffeeanto@gmail.com

† Electronic supplementary information (ESI) available: TEM/HRTEM, FESEM, EDX, XRD, XPS, ICP-OES and electrochemical characterization and stability test results of various La-doped $CoMoO_4$ catalysts. DFT structural models, DOS graphs of La-doped $CoMoO_4$ crystal structure. See DOI: https://doi.org/10.1039/d4ta06599a

and W) are a distinguished class of electrode materials explored as active catalytic/energy storage materials for different electrochemical applications, including fuel cells, HERs/OERs and supercapacitors, because of their multi-redox properties, reasonable activity/conductivity and spectacular stability, especially at high-pH values.[22–24] Recent advancements in $MM'O_4$-type catalyst materials for HER and/or OER have shown that a system consisting of mixed metal oxides/hydroxides of cobalt and molybdenum ($CoMoO_4$) is highly active in alkaline environments for water oxidation.[25–28] Despite the high activity for OER, stability under long-term electrochemical conditions has been a matter of concern since $CoMoO_4$ could inevitably undergo surface reconstruction due to the dissolution of the MoO_4^{2-} species at high-alkaline anodic/cathodic potentials.[29,30] Concurrently, the HER activity of $CoMoO_4$ has been limited due to its poor electronic conductivity and the limited number of active sites.[31–33] Besides, the overall water-splitting activity of $CoMoO_4$ has been very challenging in attaining high bifunctional activity along with long-term stability, and reports related to $CoMoO_4$ for overall water-splitting activity are scarce.

Several efforts have been put forth to address these problems *via* adopting many strategies, including the utilization of carbon-based materials as conductive supports to improve the charge transfer capacity, constructing hybrids/heterostructures to enhance intrinsic activity/conductivity, and altering electronic structures by doping.[34–38] Among the different strategies, doping of elements with high valence states could tune the electronic structure of transition metal-based electrocatalysts and influence HER/OER properties. Specifically, doping rare-earth elements in metal oxides/(oxy)hydroxides, such as La, Ce, Gd, Sm, and Yb, have been proven to be a very effective and promising strategy to enhance electrocatalytic activity and stability by increasing the surface area/active sites, improving materials conductivity, modulating electronic structure by influencing electron densities around active metal centers, optimizing binding energies of HER/OER intermediates, and reducing the overall energy barrier.[35–40] For example, Jun He *et al.* proposed high valent Ce atom introduction into amorphous iron oxyhydroxide ($CeFeO_xH_y$) nanosheets, leading to a distorted octahedral crystal structure and regulated coordination site, promoting intrinsic activity ($\eta = 250$ mV@100 mA cm^{-2}) and delivering extraordinary stability (300 h@100 mA cm^{-2}) for OER.[39] In another scenario, Huang *et al.* demonstrated electron density modulation of MoP encapsulated in a nitrogen-doped carbon matrix by La and Yb doping (RE-MoP@NC (RE = La, Yb)) toward pH-universal HER. At 10 mA cm^{-2}, the overpotentials of Yb-MoP@NC and La-MoP@NC are 136.5 and 129.3 mV, respectively, and a 12 h stability in the wide-pH range. DFT calculations substantiate that the electron density around Mo and P is tuned after La and/or Yb doping, optimizing the ΔG_{Hads} of MoP and boosting its HER activity.[40] Among rare-earth elements, La doping may offer several advantages due to its unique electronic configuration and relatively large ionic radius of La^{3+} (1.16 Å) that promotes the stabilization of the host crystal structure by preventing structural distortions and improving electrochemical performance. Furthermore, La doping can significantly enhance the electrochemical water-splitting performance of various electrocatalytic materials, particularly for OER, by tuning the electronic structure, improving active sites, and synergistic effects with the host material. However, the specific advantages and mechanisms may vary depending on the host material and doping concentration.[41–43] Inspired by the special features of La doping and previous approaches of high-valent rare-earth doping in the pioneering works, it is expected that high-valent La doping would promote intrinsic activity and impart high stability to metal oxides/metallates.

In this work, a series of La-doped $CoMoO_4$ nanostructures, with varying dopant percentages on a 3D porous and conductive Ni foam substrate, is synthesized through a one-step hydrothermal reaction. By varying the La dopant percentages, electrochemical HER and OER activities have been tuned and the best bifunctional activity is exhibited at 5% La_$CoMoO_4$ (OER: $\eta = 0.272$ V_{RHE}; HER: $\eta = 0.219$ V_{RHE}) with long-term durability under continuous electrolysis for 72 h at 20 mA cm^{-2} in a high pH media. The overall water splitting performance using 5% La_$CoMoO_4$ as the cathode and anode demanded only a low cell voltage of 1.68 V at 10 mA cm^{-2} with remarkable stability. Structural analyses and DFT calculations reveal that electron densities/electronic structure and d-band states around the active cobalt center are modulated, which optimized adsorption energies of HER/OER intermediates to optimal energy, boosting intrinsic activity and water splitting performance. To the best of our knowledge, it is the first report on a La-doped $CoMoO_4$ catalyst for overall water splitting in an alkaline medium.

2. Experimental

2.1. Chemicals and materials

Cobalt(II) nitrate hexahydrate $Co(NO_3)_2 \cdot 6H_2O$ (98%), sodium molybdate dihydrate $Na_2MoO_4 \cdot 2H_2O$ (99%), and lanthanum nitrate (99.9%) were bought from Sigma-Aldrich. Ethanol, hydrochloric acid, and potassium hydroxide were all analytic grade (AR) and purchased from Samchun Pure Chemical. All these chemicals were used without further purification. Nickel foam (NFs) (thickness 1.8 mm, 1 cm × 1 cm area) was used as a substrate. Ni foams underwent a series of cleaning steps to eliminate the oxidation layer on the surface. First, they were subjected to ultrasonic washing using a mixed solution of ethanol and acetone in equal volumes for 30 minutes. Next, the foams were sonicated in a solution of HCl with a concentration of 3 M for 15 minutes. They were then washed twice with water and ethanol, dried in air, and made ready for use.

2.2. Synthesis of the $CoMoO_4$/NF nanoarray

The $CoMoO_4$/NF nanoarray was synthesized using a hydrothermal reaction.[44] An equimolar ratio of Co $(NO_3)_3 \cdot 6H_2O$ (0.726 g, 2.5 mmol) and $Na_2MoO_4 \cdot 2H_2O$ (0.604 g, 2.5 mmol) was added to 60 mL of deionized water and stirred for 30 min to get a homogeneous solution. Next, the homogenous solution was transferred to the Teflon-lined autoclave, which had a capacity of 80 mL. NF was immersed in the above aqueous solution and

tightly closed. The autoclave was then placed in an air oven and maintained at a temperature of 180 °C for 12 h. After the reaction, violet $CoMoO_4$ crystals were grown on NF evenly, rinsed repeatedly with deionized water, followed by ethanol, and then subjected to drying at 60 °C overnight. The $CoMoO_4$ loading on the NF substrate was about ~2.0 mg cm^{-2}.

2.3. Synthesis of La-doped $CoMoO_4$ on NF

To synthesize a series of La-doped $CoMoO_4$, *x*% La_$CoMoO_4$ (*x* = 2%, 5%, 10%, and 20%), a similar experimental procedure was followed, as used for bare $CoMoO_4$ synthesis, except that a La source was introduced. In a typical procedure, stoichiometric amounts of lanthanum nitrate, cobalt nitrate, and sodium molybdate were dissolved in 60 mL of deionized water through stirring and transferred to an 80 mL Teflon-lined autoclave along with NF and heated in an air oven at 180 °C for 12 h. Then, the La-doped $CoMoO_4$ coated on NF was washed well with DI water and ethanol several times and dried at 60 °C overnight.

2.4. Electrochemical measurements

Electrochemical experiments were conducted in a standard three-electrode cell in 1 M KOH electrolyte solution using the Corrtest (CS350 in COM3) electrochemical workstation made in China. A platinum (Pt) plate served as the counter electrode, while an Hg/HgO electrode functioned as the reference electrode. The working electrode utilized was a nickel foam electrode, which was covered with a grown catalyst. All recorded potentials were referenced to the reversible hydrogen electrode (RHE) scale. Cyclic voltammetry (CV) measurements were conducted in a 1 M KOH electrolyte solution that was saturated with nitrogen (N_2). Before the electrochemical test, CV measurements were conducted at a scan rate of 50 mV s^{-1} for 100 cycles to ensure a stable response. Linear sweep voltammetry (LSV) measurements were carried out both in the cathodic sweep and anodic sweep rates at a scan rate of 5 mV s^{-1}. The double-layer capacitance (C_{dl}) was determined by measuring CV in non-faradaic regions using different scan rates (10, 20, 40, 60, 80, 100, and 120 mV s^{-1}). The electrochemical active surface area (ECSA) was calculated using the equation ECSA = geometrical surface area × C_{dl}/C_S. The specific capacitance (C_S) is a constant value (C_S = 0.040 mF cm^{-2}).[45,46] Moreover, all the acquired potentials were referenced to a reversible hydrogen electrode (RHE) using the Nernst equation: $E_{RHE} = E_{Hg/HgO} + 0.098 + 0.059 \times pH$. Electrochemical impedance spectroscopy (EIS) was studied to understand the charge-transfer kinetics. EIS measurements were carried out at the frequency range from 100 kHz to 0.1 Hz with an amplitude of 5 mV AC and an overpotential of −0.25 V_{RHE}. The long-term durability was assessed using chronopotentiometry (CP) measurements at a static current density of 20 mA cm^{-2} for 72 h. For practical applicability, the overall water-splitting activity in two-electrode cells was pursued in 1 M KOH at 298 K. Pt/C‖IrO_2 (cathode and anode) were used as the reference, and 5% La_$CoMoO_4$‖5% La_$CoMoO_4$ catalysts as the cathode and anode, respectively.

2.5. Characterization

All the synthesized catalyst materials were first analyzed for their crystal structure, purity, and phase on a powder X-ray diffractometer (Panalytical X'pert Pro, Cu Kα radiation). The microstructure and morphology were analyzed using field emission scanning microscopy (FE-SEM, HITACHI S-4800), and the nanostructure morphology was investigated using high-resolution transmission electron microscopy (HRTEM, A Philips Tecnai 20). The catalysts were analyzed for their chemical surface composition and electronic characteristics using X-ray photoelectron spectroscopy (XPS, Thermo Scientific K-α surface analysis). The XPS peak fitting and quantitative analysis were performed using the XPSPEAK41 software equipped with Gaussian/Lorentzian peak shapes. ICP-OES was performed to find wt% of the elements using PerkinElmer (OPTIMA 8300). All Raman experiments were conducted with a Raman spectrometer (model-UniDRON spectrometer) with a Rayleigh wavelength of 457 nm in the 200–2000 cm^{-1} range. To ensure the reliability and reproducibility of the acquired spectra, the Raman shift was calibrated using a silicon standard sample (520.5 cm^{-1}).

3. Results and discussion

3.1. Structure and morphological characterization

The main objective of this study is to modulate the electronic structure and strain effect of $CoMoO_4$ by systematically doping La in the $CoMoO_4$ lattice and study their effect on the electrocatalytic behavior for overall water splitting activities in high pH media. A series of La-doped $CoMoO_4$ catalysts were prepared by a single-step hydrothermal reaction (see Experimental details) by reacting lanthanum nitrate, cobalt nitrate, and sodium molybdate stoichiometrically in aqueous solution and allowing them to grow on a precleaned NF substrate, as shown in the schematic representation (Fig. 1a). The resultant 5% La_$CoMoO_4$ (for example) grew uniformly, covering the entire surface of the Ni foam (Fig. 1b, inset, and Fig. 1b and c), as evidenced by FESEM images, implying the feasibility of synthesizing an active electrocatalyst. A close examination under a high-magnification FESEM image reveals microstructures of smooth disc-shaped structures interconnected homogeneously with open gaps (Fig. 1d and e). These open gaps can be beneficial during HER/OER for easy evolution. Each disc-shaped 5% La_$CoMoO_4$ has radial and axial lengths of 0.13 and 0.7 microns, respectively. La doping in $CoMoO_4$ was confirmed by EDS spectra and elemental mapping, showing the presence of elemental peaks and homogeneous distribution of elements across the scanned area (Fig. 1f–j). One should notice that the size and morphology of $CoMoO_4$ were influenced by varying the doping content of La (Fig. S1, ESI†). Undoped or bare $CoMoO_4$ shows interconnected nanosheets of micro flower-like morphology on Ni foam. However, as the doping content increases from 2% to 20%, the thickness of nanosheets tends to increase with a decrease in lateral size as the La loading increases. Especially for 20% La_$CoMoO_4$, it appeared like an agglomeration of individual spherical/disc-shaped pellets with

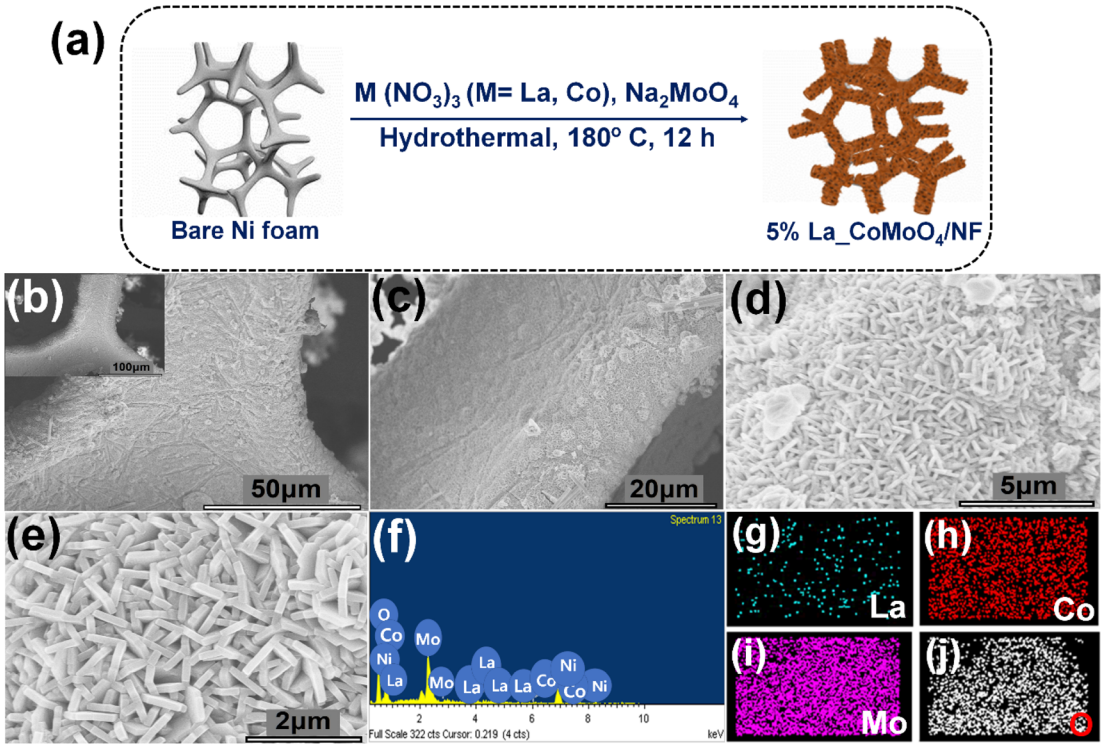

Fig. 1 (a) Schematic representation of the preparation of La-doped $CoMoO_4$, (b–e) SEM images of the as-synthesized 5% La_$CoMoO_4$, (f–j) corresponding EDS spectrum and elemental mapping analyses of elements La, Co, Mo, and O.

an average diameter of 1 to 2 microns. Among the different La-doped $CoMoO_4$, the catalyst 5% La_$CoMoO_4$ had a thick, smooth, disc-shaped morphology with a high exposed surface area. While for bare $CoMoO_4$ and 2% La_$CoMoO_4$, it appeared more like interconnected thin nanosheets, and for 10% and 20% La_$CoMoO_4$, it appeared to be agglomerated and disconnected individual pellet-shaped structures. Therefore, varying the doping content of La can influence the morphology and structure of $CoMoO_4$, which in turn can affect the electrochemical performance of the catalysts. Fig. S2† depicts the schematic of the structure evolution. First, Co, Mo, and La precursors react to form an intermediate complex ($LaCoMoO_x \cdot H_2O$). Under hydrothermal conditions, several small sheets of $LaCoMoO_4$ tend to assemble into larger nanosheets of hexagonal morphology (see TEM/HRTEM, Fig. 3) to reduce the surface energy of the system.[47] These hexagonal nanosheets grow on NF interconnected like 3D-flower-like microstructures across the surface, exposing the edges assisted by unreacted $NaNO_3$, increasing the self-assembly rate through an oriented self-assembly mechanism.[48] As the dopant content increases from 2% to 20%, the edge-thickness increases. At 20%-La doping, the 3D interconnected-flower-like structure disassembles individual pellet-shaped spherical morphology to reduce the surface energy. The varying edge size of $CoMoO_4$ nanosheets with varying La-dopant clearly depicts the increasing edge size of the hexagons as the dopant concentration increases. This may be attributed to the larger atomic radii of La (1.87 Å) than Co (1.52 Å), which enhances the lattice spacing of $CoMoO_4$ by substituting more Co with La atoms at high dopant concentrations. The FESEM images of various La-doped $CoMoO_4$ materials also confirmed the presence of elements such as La, Co, Mo, and O from elemental mapping, showing even distribution of such elements across the scanned region (Fig. S3†). Moreover, doping elements might alter the surface properties, including surface area and porosity. The BET surface area analysis was performed and as shown in Fig. S4a and c,† the BET adsorption–desorption isotherm shows a high BET surface area of ~23.7 $m^2\ g^{-1}$ for 5% La_$CoMoO_4$ among all samples and tends to decrease when the doping content increases by more than 5%. Although 2% La_$CoMoO_4$ might appear to have more surface area, the edge-surface area is quite high for 5% La_$CoMoO_4$, contributing more to the total surface area. Furthermore, the BJH pore size distribution shows a higher value for 5% La_$CoMoO_4$ (26.3 nm), suggesting increased porosity after optimal La doping than other La-doped catalysts (Fig. S4b†), which is crucial to facilitate enhanced mass and charge transfer during electrochemical HER/OER. Thus, appropriate La doping in $CoMoO_4$ optimizes the surface properties for favorable HER/OER performances.

The phase and crystal structure of the as-synthesized catalysts were studied by PXRD. Fig. 2a compares the PXRD patterns of bare and varying dopant percentages of La-doped $CoMoO_4$ from scabs of Ni foam for a clear identification since the NF substrate peaks can overwhelm the weak peaks of $CoMoO_4$. The PXRD pattern of the bare $CoMoO_4$ grown on the NF substrate exhibits three high-intensity peaks at 9.9°, 13.6°, and 29.6° (2θ). These peaks correlate to the characteristic diffractions seen from the (001), (100), and (003) crystal planes of triclinic

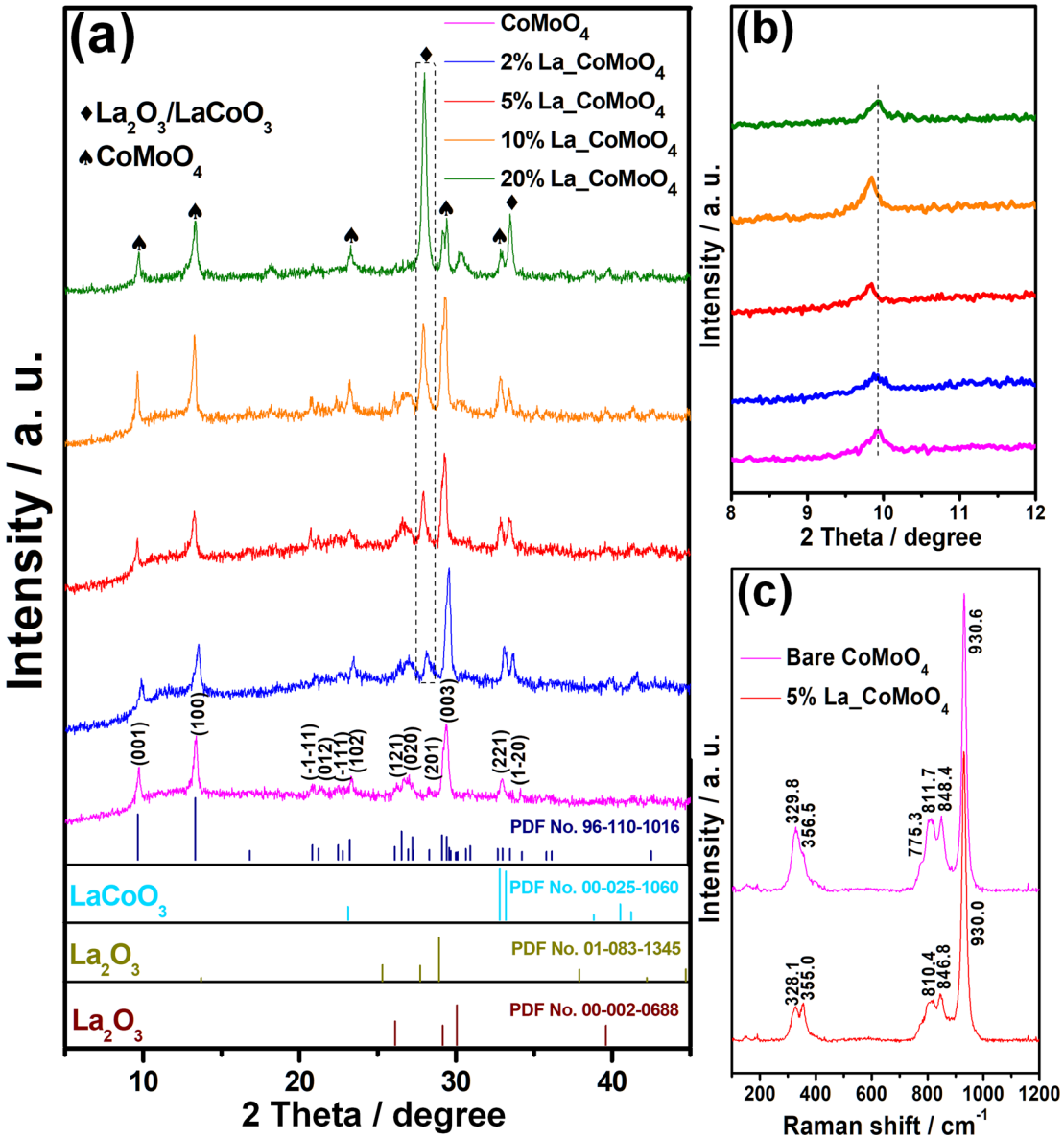

Fig. 2 (a) PXRD patterns of $CoMoO_4$, 2% La_$CoMoO_4$, 5% La_$CoMoO_4$, 10% La_$CoMoO_4$, and 20% La_$CoMoO_4$. (b) Low-angle magnified XRD patterns of $CoMoO_4$, 2% La_$CoMoO_4$, 5% La_$CoMoO_4$, 10% La_$CoMoO_4$, 20% La_$CoMoO_4$. (c) Raman spectra of bare $CoMoO_4$ and 5% La_$CoMoO_4$.

$CoMoO_4$, as identified by the JCPDS no. #96-110-1016. In comparison to the PXRD patterns of varying percentages of La-doped $CoMoO_4$ catalysts, the Braggs reflection at 9.9° (2θ) shifts to a lower angle from 2% La_$CoMoO_4$ to 10% La_$CoMoO_4$, caused by an expansion of the $CoMoO_4$ lattice due to the incorporation of a La^{3+} dopant atom (La ionic radii, 0.147 Å) into the crystal structure (Fig. 2b). This peak shift to a lower angle is due to lattice expansion caused by larger radii of La^{3+}, thus confirming the doping of La in the $CoMoO_4$ lattice. However, a further increase to 20% La concentration (20% La_$CoMoO_4$) causes a higher angle shift, indicating attaining a saturation level of the $CoMoO_4$ lattice by high La-dopant concentration.[49] Generally, the dopant atoms may occupy interstitial lattice sites instead of substitutional sites at high concentrations (20% La_$CoMoO_4$). Interstitial dopants may cause lattice compression, leading to a rightward shift of XRD peaks, independent of the dopant atom size compared to the host atom.[49] Also, La doping causes an inevitable formation of the La_2O_3 impurity phase at 28.19° (2θ), marked in a purple dotted square, and this phase intensity increases with an increase in the La doping percentage.[50]

In addition, Raman spectra provide insights into the structural changes in the $CoMoO_4$ lattice after La doping (Fig. 2c). For bare $CoMoO_4$, peaks at 329.8 and a shoulder peak at 356.5 cm^{-1} are specifically attributed to the bending vibrations of the Co–O–Mo bond. Similarly, the peaks at 811.7 and 848.4 cm^{-1} are attributed to the stretching vibrations of the O–Mo–O bond. Furthermore, the peak at 930.6 cm^{-1} is related to

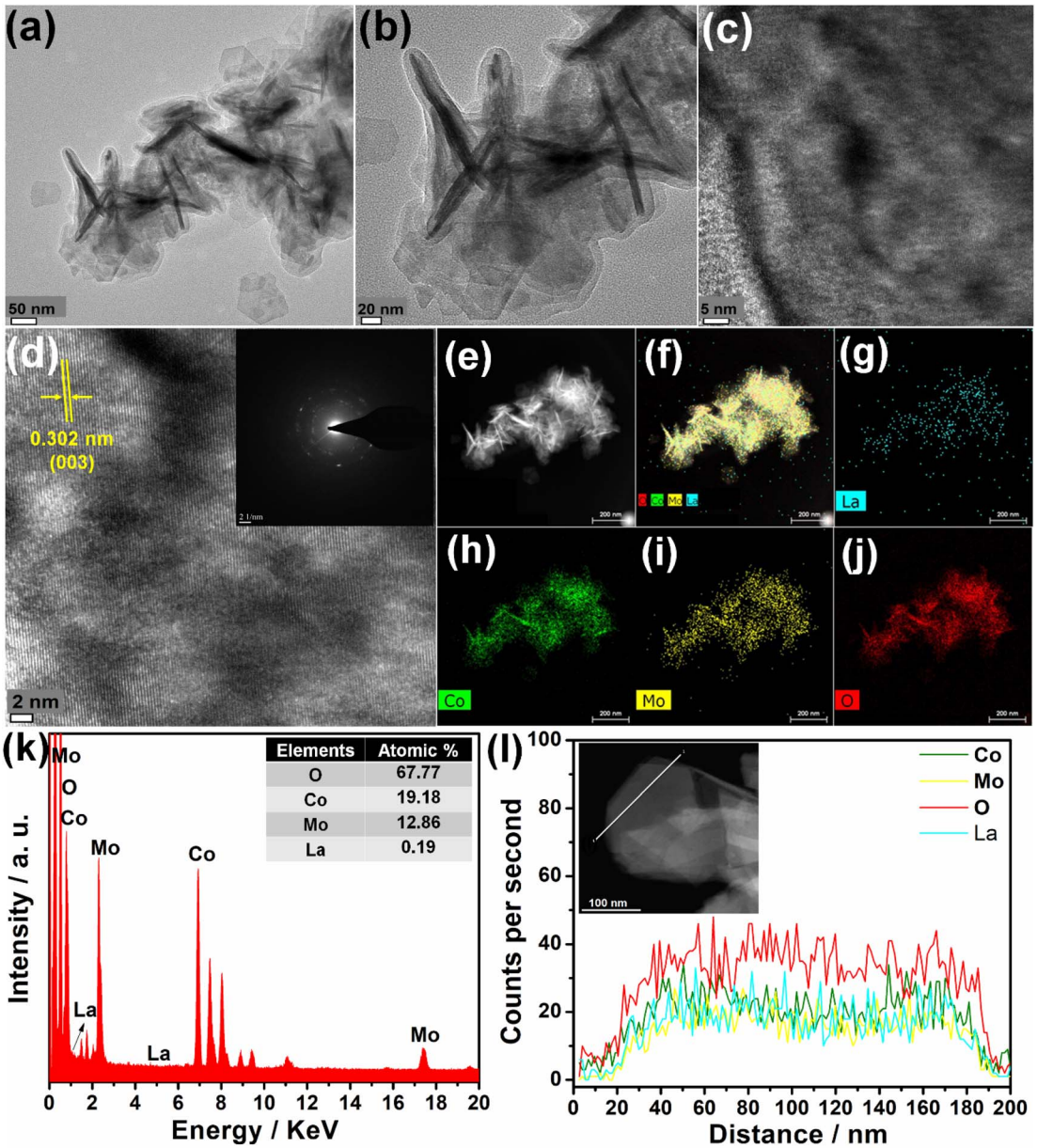

Fig. 3 Microscopic characterization of 5%_LaCoMoO$_4$. (a–d) TEM/HRTEM images of 5%_LaCoMoO$_4$; (d) inset is the SAED pattern. (e–j) HAADF-STEM image and the EDS mapping of elements La, Co, Mo and O, and (k) corresponding elemental spectra with tabulated atomic percentages of elements; (l) line profile imaging plot showing the elemental distribution on the surface of the 5%_LaCoMoO$_4$ nanosheet.

the stretching vibration of the terminal Mo=O bond, and these signatures are the characteristic peaks of the formation of the CoMoO$_4$ phase.[51] The changes in peak positions to lower wavenumbers indicate that the lattice bond lengths and angles of CoMoO$_4$ are altered after La doping for 5% La_CoMoO$_4$. This is due to the CoMoO$_4$ lattice expansion from incorporating larger-sized La^{3+} ions.[52] To get a better understanding of the La-doping effect on nanostructure morphology, TEM and HRTEM were analyzed (Fig. 3). A 5% La_CoMoO$_4$ sample grown on Ni substrate was partly dispersed in a suitable solvent and examined under a TEM microscope, consisting of plenty of hexagonal nanosheets in line with bare CoMoO$_4$ (having similar hexagons), which indicates there are not many structural changes after 5% La doping (Fig. 3a and b). Each thick nanodisc-shaped crystallite was exfoliated into thin transparent nanosheets (Fig. 3a), thus implying nanosheets are the building blocks stacked periodically to form disc-shaped structures in the 5% La_CoMoO$_4$ catalyst. We could also observe partial 1D tube-like structures coexisting. Further, the HRTEM image of 5% La_CoMoO$_4$ (Fig. 3c and d) single nanosheet surface rather reveals a lattice fringe spacing of 0.302 nm, corresponding to the (003) crystal plane of 5% La_CoMoO$_4$, showing a ~0.002 nm difference in comparison to the bare CoMoO$_4$ lattice fringe spacing at the same (003) crystal plane (Fig. S5†). This small difference of 0.002 nm suggests La element doping and corresponds to only 5% La doping. Thus, the above material

characterization evidence strongly proves La doping through our simple hydrothermal reaction. The presence and distribution of elements across the nanosheets were confirmed from the HAADF-STEM imaging mode coupled EDS (Fig. 3e–j). The homogeneous distribution of elements (La, Co, Mo, and O) in elemental mapping and the corresponding peaks in the EDS spectra prove the formation of La doping in $CoMoO_4$ for the 5% La_$CoMoO_4$ sample (Fig. 3e–k). Importantly, the EDS elemental mapping of La clearly depicts the atomic-level distribution of atoms rather than forming composites or hybrid structures. Furthermore, line profiling across the nanosheets of the HAADF-STEM (Fig. 3l) image depicts that La doping in $CoMoO_4$ exists as a single entity as alloy-type, where La atoms substitute Co sites and do not exist as core–shell structures within the nanosheet thickness. In order to identify the position of La in the $CoMoO_4$ lattice, suitable La-doped $CoMoO_4$ models through DFT studies were constructed and found that La occupies the tetrahedral sites with the La formation energy of −1.26 eV, in comparison to octahedral sites having a high formation energy of −3.95 eV (Fig. S6†).

To investigate the effect of La doping on the electronic structure, surface composition, and chemical states, XPS analyses were performed and compared (Fig. 4a–d) for the control $CoMoO_4$ and 5% La_$CoMoO_4$. XPS wide-scan survey spectrum shows significant peaks of La 3d, Co 2p, Mo 3d, and O 1s, confirming the presence of corresponding elements (Fig. 4a). The deconvoluted high-resolution XPS spectra of the Co 2p region for both control $CoMoO_4$ and 5% La_$CoMoO_4$ display spin–orbit splitting of Co 2p into a pair of doublets of Co $2p_{3/2}$ and Co $2p_{1/2}$ for Co^{3+} and Co^{2+} with associated satellite peaks. Notably, bare $CoMoO_4$ exhibits Co^{3+} and Co^{2+} peaks at binding energies (B.Es) of 780.3 and 782 eV, respectively. In comparison to 5% La_$CoMoO_4$, these peaks shift slightly to higher B.Es at 780.57 and 782.27 eV, respectively, with a B.E. difference of 0.23 eV. This B.E. shift to a higher value for 5% La_$CoMoO_4$ suggests the charge redistribution around Co atoms after La doping in the lattice. In other words, owing to the electronegativity difference and electronic interaction between La and Co, there could be a possible electron transfer from La to Co sites, causing an increase in the effective charge density as La^{3+} replaces the Co species in the $CoMoO_4$ lattice.[40] This identifies the successful doping of La in $CoMoO_4$ and consequent changes in the electronic structure of 5% La_$CoMoO_4$ *via* La incorporation. But the shift to higher B.E. of Co is attributed to a π-back donation from bridged O^{2-} to the empty orbitals of Mo centers in Co–O–Mo sites. In other words, Co^{2+} with an electronic configuration of $3d^7$ (t_{2g}^5 e_g^2) and owing to the electronegativity difference and interaction with La, the electron transfer from La to Co creates electron–electron repulsion between filled Co 2p orbitals and lone pairs of bridged O^{2-}. Therefore, a partial electron transfer further occurs from the t_{2g} orbital of Co to the empty 4d orbitals of Mo (t_{2g}^0 e_g^0) through a π-back donation from bridged O^{2-}, again creating more electropositive centers of Co, causing the B.E. to shift to higher values than bare $CoMoO_4$.[32,53] A similar trend in the electronic behavior has been observed in the deconvoluted Mo 3d spectra for bare $CoMoO_4$ and 5% La_$CoMoO_4$ (Fig. 4c). A doublet is seen corresponding to Mo $3d_{5/2}$ and Mo $3d_{3/2}$ at 231.9 and 235.1 eV for bare $CoMoO_4$ with a B.E. difference of 3.2 eV attributed to the distinctive Mo^{6+} of $CoMoO_4$ and these peaks shift toward higher B.E. by 0.12 eV after doping with La (5% La_$CoMoO_4$), suggesting changes in the Mo coordination environment.[51,52] In addition, the XPS O 1s spectra for bare $CoMoO_4$ and 5% La_$CoMoO_4$ are compared (Fig. S7†). Peaks at B.Es, 530.2 and 532.5 eV, can be assigned to the surface oxygen or lattice oxygen peaks and oxygen in adsorbed water molecules.[51] The above surface oxygen or lattice

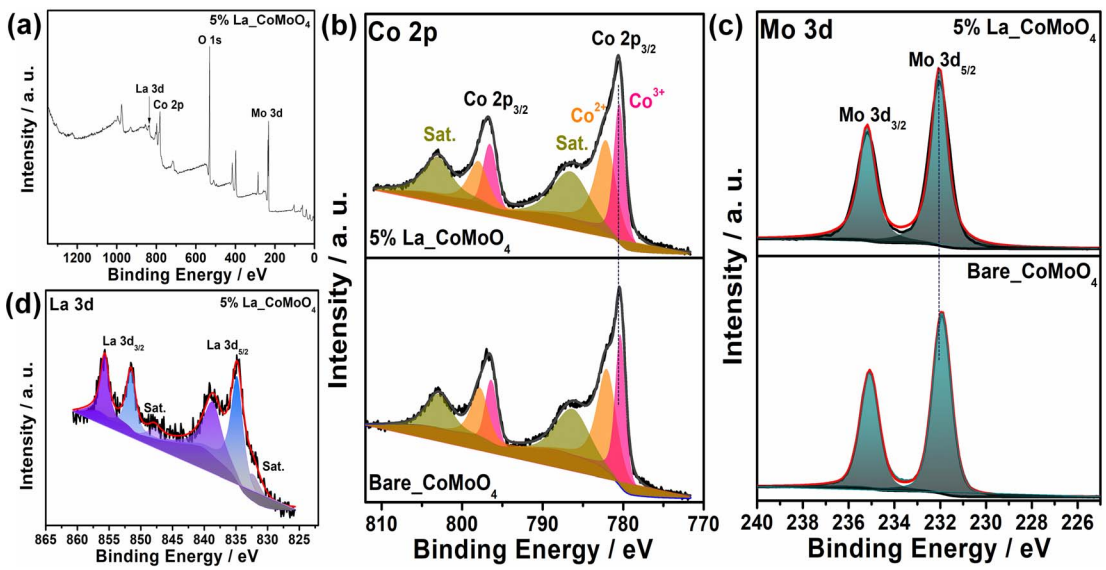

Fig. 4 XPS wide-scan survey spectra and high-resolution spectra of 5%_La$CoMoO_4$. (a) XPS wide spectra of 5%_La$CoMoO_4$. (b) Core-level Co 2p spectra of bare $CoMoO_4$ and 5%_La$CoMoO_4$. (c) Core-level Mo 3d region for bare $CoMoO_4$ and 5%_La$CoMoO_4$. (d) La 3d core-level spectra of 5%_La$CoMoO_4$.

peak has been shifted positively to 530.30 eV for 5% La_$CoMoO_4$, suggesting enhancement in the oxygen coordination environment when La is doped in the $CoMoO_4$ lattice. Similarly, the presence of La $3d_{5/2}$ and La $3d_{3/2}$ peaks (Fig. 4d) at 834.9 and 851.5 eV, respectively, and their associated satellite peaks for 5% La_$CoMoO_4$ confirm La doping with the La(III) state on the surface. Therefore, based on the aforementioned analysis, the electronic structure modulation in 5% La_$CoMoO_4$ justifies La doping in the $CoMoO_4$ lattice, and in turn, is expected to have a positive effect on the electrocatalytic properties of water-splitting reactions.

3.2. Electrochemical performance and characterization

The influence of La doping in $CoMoO_4$ on the electrocatalytic properties of OER and HER activities was evaluated using a typical three-electrode system in 1 M KOH solution (Fig. 5). The OER and HER activities of the control and varying percentages of La-doped $CoMoO_4$ electrocatalysts were probed using LSV curves (Fig. 5a and b). Firstly, the LSV curve of the bare Ni foam without catalyst showed poor OER and HER activities. However, when $CoMoO_4$ is grown on the Ni foam, the activity is increased several-fold, affirming the fact that $CoMoO_4$ is active for OER/HER in alkaline media. In comparison to the La-doped $CoMoO_4$ (varying percentages of La doping), we observe a variation in the OER/HER activities, which suggests La doping further boosts OER/HER activity.

By varying the La-dopant concentration in $CoMoO_4$ (2 to 20%), OER/HER activities can be regulated and the optimum OER/HER activity can be achieved at 5% La doping concentration (5% La_$CoMoO_4$). Therefore, for the optimal catalyst, 5% La_$CoMoO_4$, the overpotentials required to drive current densities of 20, 50, and 100 mA cm^{-2} are 0.272, 0.368, and 0.45 V_{RHE}, respectively, for OER. Meanwhile, the overpotentials demanded for HER were 0.219, 0.309, and 0.426 V_{RHE} to attain 20, 50, and 100 mA cm^{-2}, respectively (Fig. 5d). One should notice that, among different La-doped $CoMoO_4$ catalysts, too low doping (2% La_$CoMoO_4$) and very high doping (20% La_$CoMoO_4$) resulted in poor activity, almost close to the activity of bare $CoMoO_4$. Thus, the optimal OER/HER activity can be achieved only at moderate doping of La in $CoMoO_4$ (5% La_$CoMoO_4$). It is worth noting that for both OER and HER, the LSV curves follow a similar trend in the catalyst–activity relationship, signifying the homogeneity of surface composition and coherency with OER/HER reactive intermediates. To shed light on the reaction kinetics, Tafel slopes were constructed from chronoamperometry profiles of different catalysts.[54] As shown in Fig. 5c, the Tafel slope of bare $CoMoO_4$ is 113 mV dec^{-1} and for 5% La_$CoMoO_4$, the Tafel slope is reduced to 54 mV dec^{-1}. This validates that the introduction of 5% La doping in $CoMoO_4$ improves the reaction kinetics toward OER performance. A low Tafel slope value indicates an increased rate of the reaction. By varying the La-dopant content in $CoMoO_4$, Tafel slope values can be regulated in line with LSV curves. Indeed, the value of the Tafel slope gives insight into the rate-determining step (RDS). Generally, for OER, Tafel values of 120, 60, and 40 mV dec^{-1} correlate to one-, two-, and three-electron transfer reactions as the RDS. The first step is the adsorption of hydroxide, the second step is the formation of oxyhydroxides from hydroxide and the third step is the formation of oxides from oxyhydroxides.[55,56] Based on the Tafel values obtained, 5% La_$CoMoO_4$ is close to 60 mV dec^{-1}, suggesting the second step is the RDS. While for other doped catalysts (2% La_$CoMoO_4$, 10% La_$CoMoO_4$, and 20% La_$CoMoO_4$), including bare $CoMoO_4$, the Tafel values are between 60 and

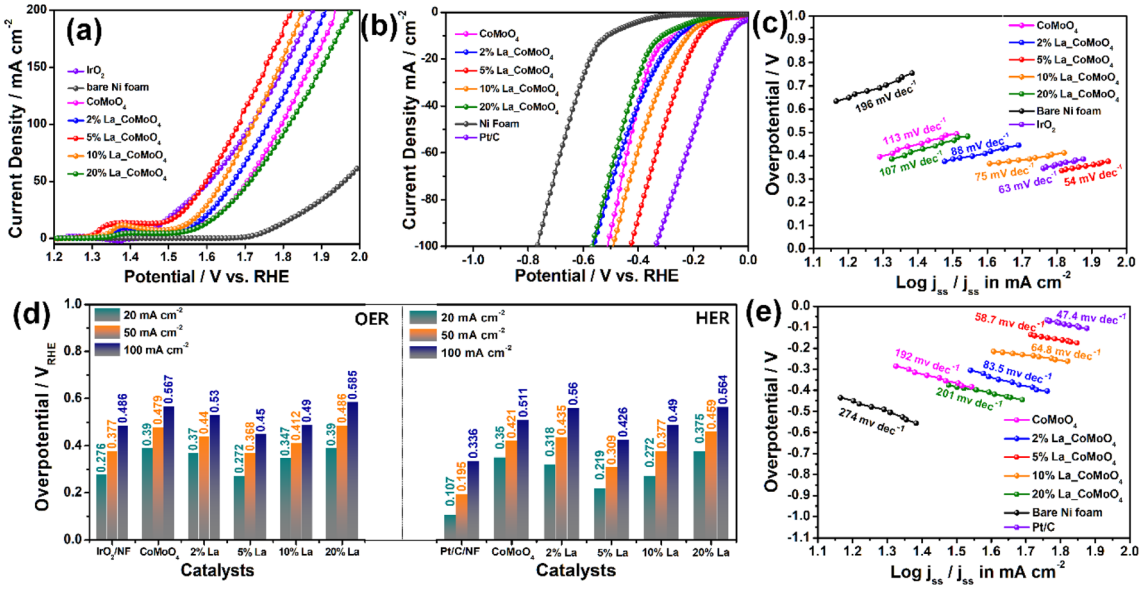

Fig. 5 Electrochemical properties of the synthesized electrocatalysts. (a) LSV responses of different La-doped $CoMoO_4$ catalysts toward the OER in 1 M KOH. (b) LSV responses of different La-doped $CoMoO_4$ catalysts toward HER in 1 M KOH. (c and e) Tafel slopes of different La-doped $CoMoO_4$ catalysts toward the OER and HER obtained *via* steady-state chronoamperometry. (d) Comparison of overpotential *vs.* different catalysts at current densities 20, 50, and 100 mA cm^{-2}.

120 mV dec^{-1}, indicating the combined first and second-step as RDS, *i.e.*, the adsorption of hydroxide and formation of oxyhydroxide. In the case of HER kinetics in alkaline solutions, three mechanistic pathways are usually followed, namely, Volmer, Heyrovsky, and Tafel steps. (1) Volmer step involves water dissociation and adsorption on the catalyst surface, followed by (2) the Heyrovsky step corresponding to electrochemical desorption and (3) the Tafel step is the recombination of the adsorbed H atoms.

$$H_2O + e^- + M \rightarrow M\text{–}H + OH^- \approx 120 \text{ mV dec}^{-1} \quad (1)$$

$$M\text{–}H + H_2O + e^- \rightarrow H_2 + M + OH^- \approx 40 \text{ mV dec}^{-1} \quad (2)$$

$$H_{ads} + H_{ads} \rightarrow H_2 \approx 30 \text{ mV dec}^{-1} \quad (3)$$

In accordance with the previous studies, Tafel slopes >120 mV dec^{-1} suggest the Volmer step as the RDS, while Tafel slopes of 40 or 30 mV dec^{-1} indicate Heyrovsky or Tafel as the RDS.[51] Based on the obtained Tafel values from chronoamperometry, 5% La_CoMoO$_4$ has a Tafel slope of 58.7 mV dec^{-1} (Fig. 5e), which is between Volmer and Heyrovsky steps, thus following the Volmer–Heyrovsky mechanistic pathway, including for the moderately doped catalysts (2% La_CoMoO$_4$ and 10% La_CoMoO$_4$). However, for excessive doping (20% La_CoMoO$_4$) and bare CoMoO$_4$, Tafel slopes exceed 120 mV dec^{-1}, implying Volmer as the RDS, *i.e.*, reaction kinetics involves water dissociation and adsorption at the catalyst surface. Thus, optimal doping necessitates improved reaction kinetics toward HER/OER. A comparison of overpotentials and Tafel slopes of recently reported rare-earth doped catalysts with our catalysts for OER and HER is depicted in Fig. 6e and f. To evaluate the charge-transfer kinetics of the prepared electrocatalysts, EIS measurements were performed (Fig. 6a). The Nyquist plots fitted with equivalent circuits and the EIS results are presented in Fig. S8 and Tables S1–S4, ESI.† The Nyquist plots of all the catalysts follow identical shapes, which signify a similar charge-transfer process on the catalyst surface, regardless of doping concentration. From the EIS fitting parameters, the ECSA normalized charge-transfer resistance (R_{ct}) of 5% La_CoMoO$_4$ is low (0.025 and 0.071 ohm cm^2) compared to other catalysts toward OER and HER (Fig. 6a). This suggests that the appropriate doping of La ion decreases charge-transfer impedance and improves the charge-transfer rate of 5% La_CoMoO$_4$, effectively promoting OER/HER kinetics.

The electrochemical surface areas (ECSAs) of the La-doped CoMoO$_4$ samples were determined by measuring their double-layer capacitance (C_{dl}) roughly from the CVs in the non-faradaic region, with various scan rates as shown in (Fig. S9 and S10, ESI†). According to Fig. 6b, the ECSA rose to higher values as the La doping increased and then decreased as the doping amount exceeded the optimal La-dopant concentration. Specifically, the ECSA increased from 54.5 cm^2 for CoMoO$_4$ to 73 cm^2 for 2% La_CoMoO$_4$ and reached its highest value of 104 cm^2 for 5% La_CoMoO$_4$. With further increase in the percentage of La, the C_{dl} reduced to 101 cm^2 for 10% La_CoMoO$_4$ and 30.1 cm^2 for 20% La_CoMoO$_4$. The ECSAs for HER also showed a similar trend on La_doped CoMoO$_4$ samples; thus, the ECSA trend of various electrocatalysts in the cathodic and anodic non-faradaic regions mirrored electrochemical activity. The result suggests that incorporating La as a dopant is a fantastic way to improve active site exposure and ECSA of CoMoO$_4$, and in turn, reflects that a larger ECSA of 5% La_CoMoO$_4$ ensured a greater number of active sites, promoting the adsorption of reactive

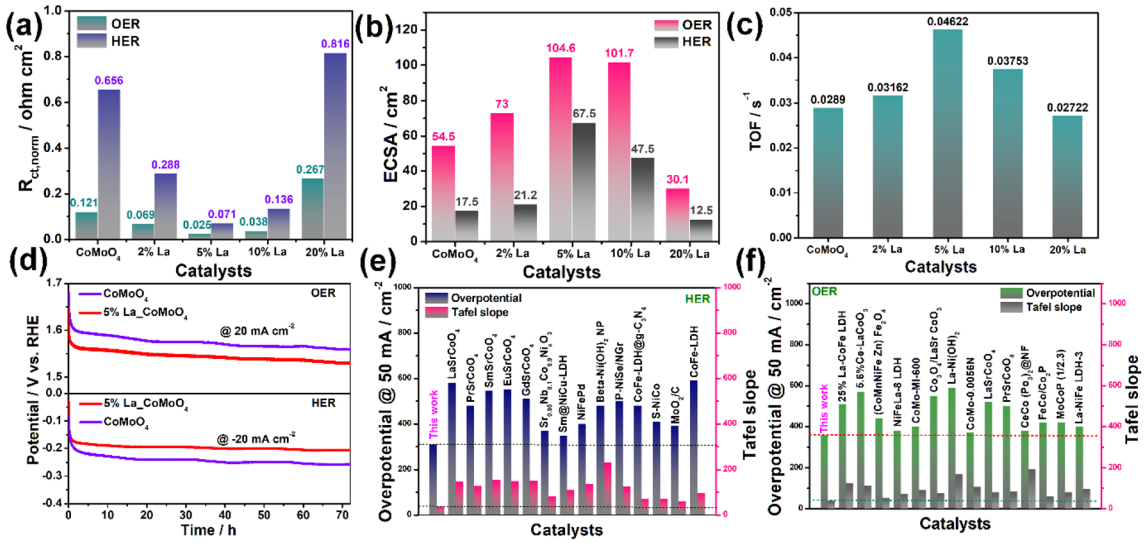

Fig. 6 Electrochemical properties of the as-synthesized electrocatalysts. (a) ECSA normalized charge-transfer resistance comparison plots of different La-doped CoMoO$_4$ catalysts estimated from Nyquist plots toward the OER and HER. (b) ECSA of various La-doped CoMoO$_4$ catalysts comparison plots computed from the CVs at the non-faradaic regions toward the OER and HER. (c) TOFs at 1.7 V_{RHE} comparison plot among various La-doped CoMoO$_4$ catalysts. (d) Chronopotentiometry profile comparison of bare CoMoO$_4$ and 5% La_CoMoO$_4$ for 72 h duration in 1 M KOH at $\eta = 1.7$ V_{RHE} and -0.1 V_{RHE} toward the OER and HER (e and f) comparison of overpotential at 50 mA cm^{-2} and Tafel slope values of various competitive HER/OER electrocatalysts reported in the literature with our present work.

intermediates with fast charge transfer and efficient diffusion of the electrolyte, consequently boosting the electrocatalytic water splitting performance. This fact was proved by estimating TOFs of different electrocatalysts as a direct measure of evaluating the intrinsic properties of electrocatalysts (Fig. 6c). TOFs at 1.7 V_{RHE} apparently proved 5% La_$CoMoO_4$ manifesting the highest value of 0.0462 s^{-1} of O_2, almost two times higher gas evolution per active site per time than the bare $CoMoO_4$ catalyst, thus proving the efficacy of 5% La doping in $CoMoO_4$. The different TOFs for different electrocatalysts are due to the varying La-dopant percentages over $CoMoO_4$, effectively changing the surface accumulated charges, especially during the OER process.

This accumulation of charges strongly influences the adsorption/desorption of electroactive species during electrocatalysis. To elucidate this, the surface accumulated charge at various La-doped percentages over $CoMoO_4$ catalysts was estimated from the redox peaks of CVs, including the undoped $CoMoO_4$ catalyst (Fig. S11, ESI†). It is worth mentioning that La doping in $CoMoO_4$ increases the reduction area compared to bare $CoMoO_4$ catalyst, implying the charge accumulation on the catalyst surface increases after La doping and this may proportionally enhance the OH^- adsorption over the catalyst surface for enhanced catalytic activity.[56] However, we observed a different trend in the activity, *i.e.*, increasing the La-dopant beyond 5% showed a decline in activity. The estimated charges of different electrocatalysts from the redox peak were plotted against the current density at 1.7 V_{RHE}, resulting in a volcanic-shaped relation, wherein 5% La_$CoMoO_4$ is at the summit (Fig. S12, ESI†). It is important to note that charge accumulation increases with an increase in the La-dopant percentage, allowing effective adsorption of OH^- species. However, this would not favor an increasing activity trend with an increase in La-dopant percentage since the accumulation of positive charges would disfavor the easy release of O_2 during OER kinetics. Thus, optimal accumulation of charges on the catalyst surface is necessary to balance the adsorption and desorption processes. Accordingly, 5% La_$CoMoO_4$ holds optimal charge accumulation to maximize interactions with the OH^- species by balancing easy adsorption and desorption processes with optimal energy to impart high electrocatalytic activity in agreement with the Sabatier principle of adsorption. The above electrochemical characterization clearly proved enhancement in active sites and consequent electrocatalytic properties after electronic structure modulation of $CoMoO_4$ through La doping.

In order to assess the electrochemical stability of the optimal 5% La_$CoMoO_4$ electrocatalyst as well as to portray the practicability and long-term chronopotentiometry (CP) in both anodic and cathodic potentials was carried out under a static current density of 20 mA cm^{-2}. As shown in Fig. 6d, 5% La_$CoMoO_4$ manifested a stable and non-fluctuating CP profile both in the anodic and cathodic potentials throughout 72 h, demonstrating its spectacular long-term stable performance without any noticeable decay under diverse and harsh electrochemical conditions, proving its viability for water-splitting applications. Such a stable performance could be attributed to the contribution of the La-dopant, which not only enhances the activity but also maintains high structural stability under electrochemical conditions. As proven by Jun He *et al.* in one of the studies, rare-earth metal Ce-doping in FeOOH demonstrated a high-stable performance for over 100 h in both three-electrode and two-electrode performances, attributed to a change in the coordination structure of FeOOH *via* Ce-doping.[39] In the present case, La doping could alter the electronic structure (as proved by XPS) and coordination geometry of $CoMoO_4$, which significantly contributed to electrochemical stability during continuous electrolysis. For comparison, long-term stability for bare $CoMoO_4$ was accomplished for up to 72 h under identical conditions and compared with 5% La_$CoMoO_4$. It can be clearly identified that bare $CoMoO_4$ exhibits attenuated chronopotentiometry profiles, indicating reduced stability. To prove the structural stability endured by 5% La_$CoMoO_4$, FESEM images post-catalysis (72 h CP) reveal identical morphology to that of the initial as-prepared catalyst (Fig. 1b) on the NF substrate without any detachment of catalyst from the surface. Furthermore, EDS elemental mapping images proved the existence and homogeneous elemental distribution (La, Co, Mo, and O) without significant leaching or loss, signifying its excellent stability in alkaline media (Fig. S13, ESI†).

3.3. Two-electrode water-splitting performance

The fascinating dual capabilities of 5% La_$CoMoO_4$ for both the HER and OER have inspired us to develop a two-electrode water-splitting electrolyzer to realize its industrial applicability as a potential catalyst in anion-exchange membrane water electrolyzer (AEMWE). The water-electrolyzer was assembled by employing 5% La_$CoMoO_4$ as both the cathode and anode (5% La_$CoMoO_4$‖5% La_$CoMoO_4$) in the two-electrode configuration using 1.0 M KOH electrolyte to evaluate its bifunctional electrocatalytic activity. The 5% La_$CoMoO_4$ bifunctional electrocatalyst demanded a low cell voltage of 1.76 V to drive 20 mA cm^{-2}, surpassing the commercial Pt/C‖IrO_2/C cathode and anode catalysts with a cell voltage of 1.86 V under identical conditions (Fig. 7a). However, our bifunctional electrocatalyst cell voltage (1.76 V) is higher than the theoretical reversible potential of the water-splitting reaction (1.23 V). Still, it is comparable to the performance of various rare-earth doped electrocatalysts and other state-of-the-art materials (Fig. 7d). The graphical representation in Fig. 7c illustrates the effect of La doping in boosting the overall water-splitting activity of a 5% La_$CoMoO_4$ catalyst. From a practical point of view, the long-term stability of the 5% La_$CoMoO_4$‖5% La_$CoMoO_4$ system is essential. Fig. 7b illustrates the long-term stability of the 5% La_$CoMoO_4$‖5% La_$CoMoO_4$ system producing a stable voltage profile at 1.8 V attained at 20 mA cm^{-2} with a voltage retention of ~99% during continuous electrolysis of 45 h. Contrary to this, the Pt/C‖IrO_2/C system showed a drastic decline in cell potential within a few hours of operation, proving its instability under practical conditions.

3.4. Post-catalysis: structural and morphological stability

The structural and electrochemical stability of 5% La_$CoMoO_4$ (post-catalyst) were probed by various microscopic and

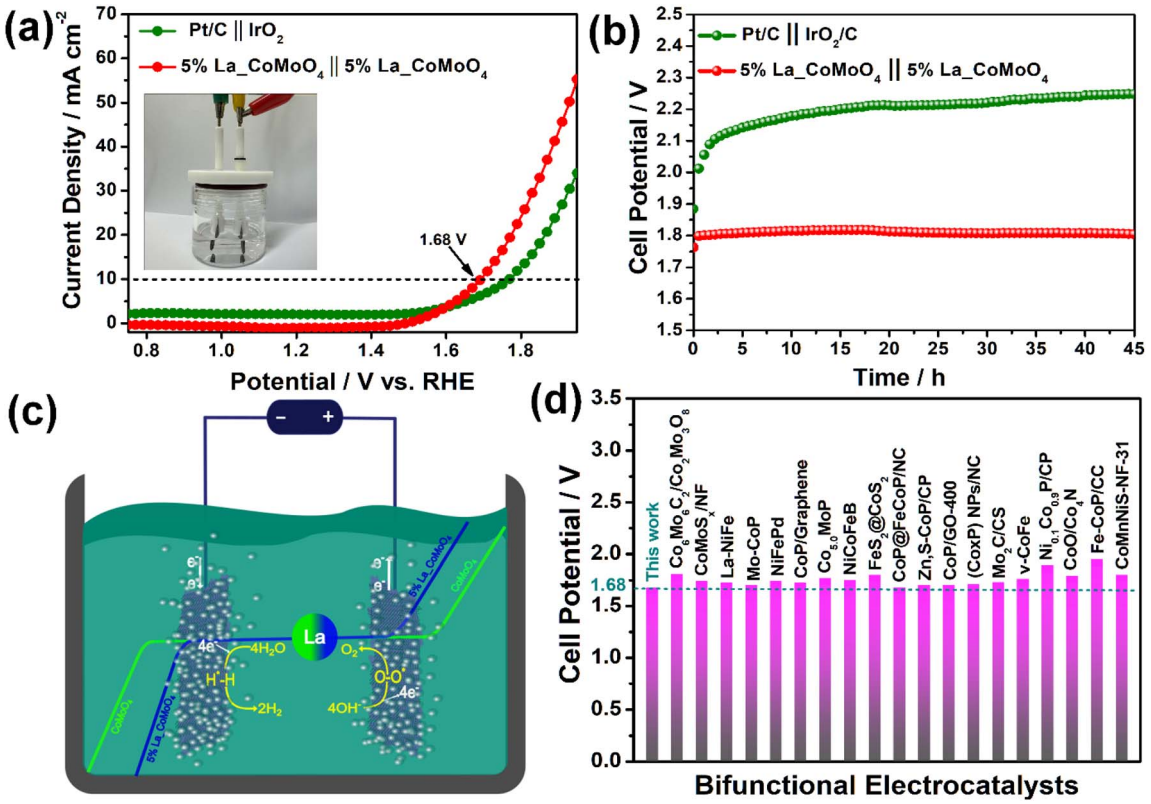

Fig. 7 Two-electrode electrochemical properties of 5% La_$CoMoO_4$. (a) LSV response of 5% La_$CoMoO_4$||5% La_$CoMoO_4$ and commercial Pt/C||IrO_2/C cathode and anode toward overall water splitting in 1 M KOH media, (b) chronopotentiometry stability profiles of 5% La_$CoMoO_4$||5% La_$CoMoO_4$ and commercial Pt/C||IrO_2/C cathode and anode for 72 h duration in 1 M KOH at an applied $\eta = 1.7$ V_{RHE} and 1.78 V_{RHE} in a two-electrode water electrolyzer cell, and (c) graphical representation of the overall water splitting activity comparison of bare and La-doped $CoMoO_4$ catalyst. (d) Bifunctional electrochemical comparison performance of various competitive electrocatalysts reported in the literature with our present work.

spectroscopic analyses of both the (anode/cathode) electrodes of the two-electrode system, and this post-catalysis characterization is a very crucial analysis and deciding factor in determining the intrinsic active sites, structural and morphological lability of the electrocatalysts. Firstly, to prove the morphological stability endured by 5% La_$CoMoO_4$, the post-catalysis FESEM images (72 h CP) reveal identical morphology to that of the initial as-prepared catalyst (Fig. 1b) on the NF substrate without any significant detachment of catalysts from the substrate surface. Furthermore, the EDS elemental mapping images prove the existence and homogeneous elemental distribution (La, Co, Mo, and O) without significant leaching or loss, indicating its excellent stability in alkaline media (Fig. S13, ESI†). Importantly, since the anode and cathode catalyst employed in the two-electrode system is 5% La_$CoMoO_4$, the post-catalysis characterization of the cathode/anode after 72 h stability is crucial to probe the structural changes occurring at the cathode and anode. Firstly, XPS analyses of both the anode and cathode post-catalysis materials (5% La_$CoMoO_4$) were investigated and compared to the initially prepared catalyst (Fig. S14, ESI†).

The deconvoluted high-resolution Co 2p spectra of post-catalysts 5% La_$CoMoO_4$ anode and cathode show a pair of doublets corresponding to Co $2p_{3/2}$ and Co $2p_{1/2}$ spin–orbit splitting relative to the initial Co 2p region of 5% La_$CoMoO_4$ catalyst (Fig. S14a, ESI†). However, peaks due to Co^{3+} and Co^{2+} are shifted negatively by 0.34 eV for the anode and 0.91 eV for the cathode, respectively, in comparison to the 5% La_$CoMoO_4$ catalyst, suggesting a possible surface structural alteration. In addition, the Co^{3+}/Co^{2+} area ratios are even regulated, showing a higher ratio for the 5% La_$CoMoO_4$ anode (1.62) than the cathode catalyst (1.41). In other words, the increased Co^{3+}/Co^{2+} area ratio of the 5% La_$CoMoO_4$ anode validates more exposed Co^{3+} sites on the catalyst surface. Several *in situ operando* studies have demonstrated that during a higher anodic bias, the catalyst surface structurally transforms to metal(oxy) hydroxide *via* a metal hydroxide intermediate, which is the key to promoting OER.[57–60] The negative shifts of the Co^{3+}/Co^{2+} peaks and the increasing Co^{3+}/Co^{2+} ratio are thus believed to generate partial surface reconstruction as CoOOH on the 5% La_$CoMoO_4$ anode catalyst surface.[57] This phenomenon of surface reconstruction is facilitated by the leaching Mo as MoO_4^{2-} ions, causing structural evolution of $CoMoO_4$ to CoOOH, which is verified by the negative peak shifts in Mo 3d regions (Fig. S14b, ESI†) and reduced atomic% of Mo (after 72 h stability in comparison to the initial catalyst) as determined from the FESEM_EDS spectra (Fig. S13, ESI†). The decreased Co^{3+}/Co^{2+} area ratio of 5% La_$CoMoO_4$ cathode could suggest the

formation of $Co(OH)_2$ under strong reduction conditions (Fig. S14a†). However, the negative XPS peak shifts of Co (cathode/anode) imply surface reconstruction to CoOOH and $Co(OH)_2$ accumulated charge redistribution on Co sites due to the partial dissolution of MoO_4^{2-} causing a negative shift to lower B.Es.[61,62] It is worth noting that the reduced molybdenum content accounts for only ~55% leaching into the electrolyte for the whole bulk structure based on ICP-OES analyses (Table S5†). In comparison to the several reported works on MoO_4^{2-} leaching effect in transition metal-based catalysts,[57–59,63,64] it accounts for more than ~85–90% leaching. Thus, the low leaching of MoO_4^{2-} species in our case can be ascertained due to the high structural stability endured by La doping, which stabilizes the bulk crystal structure of $CoMoO_4$ against complete leaching of the bulk materials despite exposure to higher anodic bias.

Intriguingly, as shown in Fig. S14c, ESI,† the deconvoluted La 3d spectra reveal significant La $3d_{5/2}$ and La $3d_{3/2}$ peaks for the 5% La_$CoMoO_4$ anode post-catalyst, proving the existence of La^{3+} dopant in the $CoMoO_4$ lattice even after long-term stability without any significant leaching of dopant species, suggesting high-structural and integral stability of 5% La_$CoMoO_4$. However, the 5% La_$CoMoO_4$ cathode displays a partial reduction in La $3d_{5/2}$ and La $3d_{3/2}$ peak regions, likely due to the partial dissolution of La^{3+} ions during electro-reduction at the cathode. In the O 1s spectrum of the 5% La_$CoMoO_4$ anode, the lattice metal–oxygen peak has been positively shifted by 0.18 eV and the peak at 531.3 eV can be assigned to metal–hydroxyl groups, and/or lattice oxygen vacancies. The increased intensity of the metal–hydroxyl peak for the 5% La_$CoMoO_4$ anode compared to the initial 5% La_$CoMoO_4$ catalyst is attributed to CoOOH formation at the surface under anodic conditions. Meanwhile, the lattice metal–oxygen peak has been shifted more negatively to 529.4 eV for the 5% La_$CoMoO_4$ cathode post-catalyst, along with an increased peak intensity of the metal–hydroxyl and/or lattice oxygen peak at 530.9 eV (Fig. S14d, ESI†). This indicates higher oxygen vacancy formation, as well as diminished lattice oxygen peak, which is evident under high cathodic potential. Based on the aforementioned XPS analyses, it is important to emphasize that for the 5% La_$CoMoO_4$ anode post-catalyst, despite its partial surface reconstruction, La-dopant promotes structural stability when compared to 5% La_$CoMoO_4$ cathode post-catalyst, under long-term electrochemical conditions.

The structural stability was further corroborated by Raman analyses, as depicted in Fig. S15, ESI.† The Raman spectra of the initial 5% La_$CoMoO_4$ and cathode/anode_post-catalysis catalysts are compared. Both the cathode and anode catalysts, after 72 h stability tests, exhibit major structural changes compared to the initial 5% La_$CoMoO_4$. For the anode_post catalyst, weak broad bands emerge between 400 and 600 cm^{-1} in comparison to the initial 5% La_$CoMoO_4$. These broad bands at 462 and 564 cm^{-1} are attributed to the E_g and A_{1g} modes of Co–O vibrations in CoOOH, leading to surface reconstruction on the catalyst surface, which are in line with XPS analyses and act as active sites for promoting high catalytic activity. The absence of peaks at 333, 360, 804, 849, and 932 cm^{-1} suggests the leaching of MoO_4^{2-} in the electrolyte. However, for the cathode_post catalyst, peaks at 690 and 893 cm^{-1} are indexed to $Co(OH)_2$ and re-adsorbed MoO_x moieties, yielding circumstantial evidence to the different phenomena, which are further explained in the *in situ* Raman analyses.

3.5. *In situ* Raman analyses

In situ Raman analyses were investigated to determine the dynamics of structural reconstruction on 5% La-doped $CoMoO_4$ (optimal catalyst). *In situ* Raman analyses were probed in HER and OER potential regions under identical conditions for bare $CoMoO_4$ and 5% La-doped $CoMoO_4$ catalysts, as shown in Fig. 8a–c. The Raman spectra of bare $CoMoO_4$ (dry state) were recorded under successively increasing potential starting from 1.20 to 1.60 V (*versus* RHE) with a 0.05 V step. In the case of bare $CoMoO_4$ (Fig. 8a), pristine $CoMoO_4$ (dry state) shows Raman peaks characteristic of $CoMoO_4$ as discussed previously.[65] Under OCP conditions, new Raman signals at ~456 cm^{-1} correspond to the E_g vibrational mode of CoOOH.[53,60,65,66] Further, reports claim that surface reconstruction to CoOOH is triggered by the transformation of Co^{2+} to Co^{3+} under anodic bias, accompanied by exsolution of Mo as MoO_4^{2-} in KOH electrolyte[61] However, in bare $CoMoO_4$ under increasing anodic bias, only partial dissolution is noticeable. The peak at ~931 cm^{-1} attributed to the Mo=O stretching frequency is discernible at all positive potentials and a newly developed peak at 895 cm^{-1} is assigned to monomolybdate ions in the electrolyte solution due to partial dissolution of Mo as MoO_4^{2-}.[67] Furthermore, a broad peak with a high intense peak observed at ~320 cm^{-1} due to Mo–O bending vibrations slightly redshifted to the pristine indicates a more disordered structure of CoOOH as the disordered amorphous structure features unsaturated active centers with improved active sites promoting the intrinsic catalytic activity.[68,69] Meanwhile, a shoulder peak at 806 cm^{-1} and a small peak at 854 cm^{-1} remain intact, as observed for the pristine $CoMoO_4$ dry sample. Moreover, the E_g vibrational mode of CoOOH (~456 cm^{-1}) in bare $CoMoO_4$ is less pronounced with applied potential compared to that of 5% La-doped $CoMoO_4$, as discussed below (the CoOOH peak is more pronounced and dominant, as shown in Fig. 8b). The above observations indicate that under an applied anodic bias, for bare $CoMoO_4$, the transition to only partial CoOOH active phase formation at the electrode surface accounts for its poor OER activity.

On the other side, for 5% La_$CoMoO_4$ (Fig. 8b), the Co–O vibrations at ~464 and ~574 cm^{-1} of γ-CoOOH becomes more prominent with red-shifting of peaks as a function of anodic bias, suggesting the evolution of the more disordered γ-CoOOH phase at the electrode surface in promoting enhanced OER and optimizing OER intermediate binding energy.[70] Notably, the La_$CoMoO_4$ catalyst undergoes surface restructuring upon immersion in the electrolyte solution without applied potential bias, demonstrating that the as-prepared sample acts as a pre-catalyst in this reaction. Notably, a peak at ~501 cm^{-1} (Fig. 8b) is visible under OCP; however, it is not obvious during a stepped potential sweeping (Fig. 8b). A previous report suggests that the 501 cm^{-1} band is related to the β-CoOOH phase.[53] Therefore,

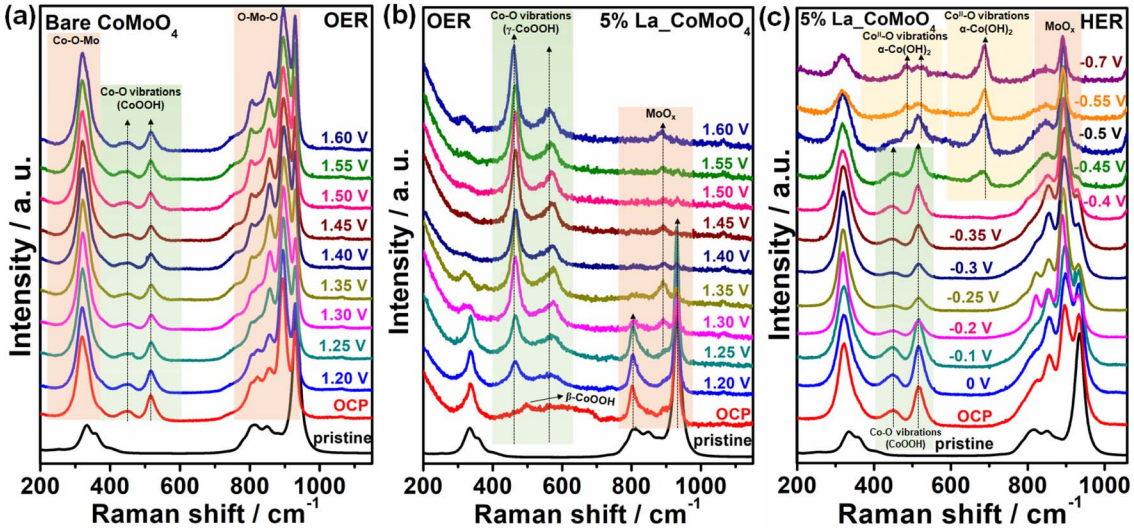

Fig. 8 Pristine and *in situ* Raman spectra of (a) bare $CoMoO_4$ for the OER, (b) 5% La_$CoMoO_4$ for the OER, (c) 5% La_$CoMoO_4$ for the HER.

two different types of Co species are generated from the oxidation of $CoMoO_4$: β-CoOOH with a Raman peak at 501 cm^{-1} under an OCP condition that disappears upon applied potential, and γ-CoOOH with Raman peaks at ~464 and ~574 cm^{-1} under different applied potentials (from 1.20 V_{RHE} to 1.60 V_{RHE}). Therefore, at higher potentials, γ-CoOOH active sites are formed at two different positions, suggesting a significant structural transformation process. Generally, the formation of γ-CoOOH at the electrode surface is believed to catalyze OER in agreement with previous studies.[53,70] Notably, the γ-CoOOH active sites are more pronounced; thus, the dominant active-phase γ-CoOOH is more favorable to the OER activity of La_$CoMoO_4$ compared to bare $CoMoO_4$ (CoOOH peak is less pronounced). More importantly, peaks at ~336 and 931 cm^{-1} attributed to Mo=O bending/stretching frequencies are prevalent only up to 1.25 V_{RHE}. A further applied potential at 1.30 V_{RHE} facilitates rapid dissolution of MoO_4^{2-} and peaks attributed to Mo–O/Mo=O modes vanished at 1.40 V_{RHE}. However, the dissolved molybdate ions in the electrolyte could be coupled to γ-CoOOH/La$CoMoO_4$ under higher applied potentials, forming MoO_x/γ-CoOOH hybrids as a real hybrid catalyst for OER, especially at higher applied potentials as demonstrated by the appearance of a less pronounced peak at ~892 cm^{-1}. Beyond 1.40 V_{RHE}, the formation of γ-CoOOH is substantial and remains significant until 1.6 V_{RHE}. Therefore, the rapid Mo dissolution is facilitated after La doping in $CoMoO_4$, which is more likely favorable for promoting faster surface reconstruction kinetics in an alkaline environment, thus exposing the abundant active sites of γ-CoOOH as the major active component. Since γ-CoOOH catalyzes OER, a rapid formation of γ-CoOOH is more desirable for enhanced OER kinetics. Thus, La doping modulates the electronic structure of $CoMoO_4$ and facilitates the rapid generation of abundant active sites at the electrode surface under OER conditions.

To further investigate the dynamics of structural reconstruction on 5% La-doped $CoMoO_4$, *in situ* Raman analyses were investigated under HER conditions. For the 5% La_$CoMoO_4$ sample, as shown in Fig. 8c, similar peak features are observed (as shown for bare $CoMoO_4$, Fig. 8a) starting from OCP to −0.4 V_{RHE} toward cathodic sweeping potentials, *i.e.*, MoO_4^{2-} dissolution is even noticeable under a cathodic bias. As the sweep potential gradually shifts to more cathodic potentials, Co–O vibrations of CoOOH (~456 cm^{-1}) begin to diminish in intensity. At −0.50 V_{RHE}, CoOOH vibrations disappear, and new broad signals between 470 and 530 cm^{-1} appear along with another additional peak at ~686 cm^{-1}, which can be indexed to the Co–O bending/stretching vibrations of disordered or defective α-$Co(OH)_2$ phase.[60] This is due to strong reduction potentials converting Co^{3+} state to Co^{2+} reacting with OH^- to generate $Co(OH)_2$ *in situ* ($Co^{2+} + OH^- \rightarrow Co(OH)_2$) and remains noticeable up to −0.70 V_{RHE},[53,61] implies surface realteration at the electrode surface by α-$Co(OH)_2$ under high cathodic sweeps. Meanwhile, the dissolved molybdate ions in the electrolyte can be coupled to α-$Co(OH)_2$/La$CoMoO_4$ under higher applied cathodic potentials, forming MoO_x/α-$Co(OH)_2$ hybrids on the 5% La_$CoMoO_4$ surface as a real hybrid catalyst for HER, especially at higher negative potentials as evidenced by the non-fading peak at 892 cm^{-1}. The electronic interaction between MoO_x and α-$Co(OH)_2$ leads to highly active and stable Co–O–Mo^{6+} species promoting the transfer of electrons at the Mo–O sites, thus optimizing the binding energies of H*/H_2O adsorption for efficient HER process. Also, the synergetic interactions in MoO_x/α-$Co(OH)_2$/5% La_$CoMoO_4$ hybrids might contribute to much enhanced HER activity.[61,62] Based on the above analyses, *in situ* Raman sheds light on the dynamic evolution of the surface reconstruction process and critical formation of real active sites on the electrode surfaces. It is worthwhile to note that under anodic bias, La doping is favorable to the rapid dissolution of Mo species and surface reconstruction to the more active γ-CoOOH phase on the 5% La$CoMoO_4$ electrode, boosting OER performance. Meanwhile, in bare $CoMoO_4$, only partial dissolution of Mo is evident, leading to the limited

generation of active CoOOH sites. Contrarily, under cathodic bias, the initially formed γ-CoOOH (~456 cm^{-1}) gradually converts to α-$Co(OH)_2$, and the exsolution of Mo as MoO_4^{2-} recombines to form $MoO_x/Co(OH)_2$/5% La_$CoMoO_4$ hybrids under strong reduction potentials and act as the active component for HER.

3.6. Density functional theory (DFT) studies on La-doped $CoMoO_4$ catalysts

Density functional theory (DFT) calculations were carried out to acquire insights into the electronic effects of the $CoMoO_4$ catalyst induced by La doping at the atomic level and their impacts on the adsorption energies of reactive intermediates, which might help to comprehend the exceptional HER and OER performance of 5% La_$CoMoO_4$ under alkaline conditions.

The optimized supercell models of bare $CoMoO_4$ and La-doped $CoMoO_4$ (5% La_$CoMoO_4$) structures with OOH and OH* coverage are shown in Fig. 9a, b and S16a–d, ESI.† The free energies are calculated using the computational hydrogen electrode model, given by Nørskov *et al.*[71] For OER activity, surface Co sites near the La-dopant are considered as the active sites for the adsorption of reactive intermediates. On this surface, the OOH* intermediate does not form and dissociates into O* and OH* due to the unsaturated Co atom, thereby resulting in a high overpotential of 5.2 V. This validates the experimental result that pure $CoMoO_4$ is not OER efficient. Further, for 5% La_$CoMoO_4$, two possible sites are tested for doping. Co atom on the surface and the second layer is tested

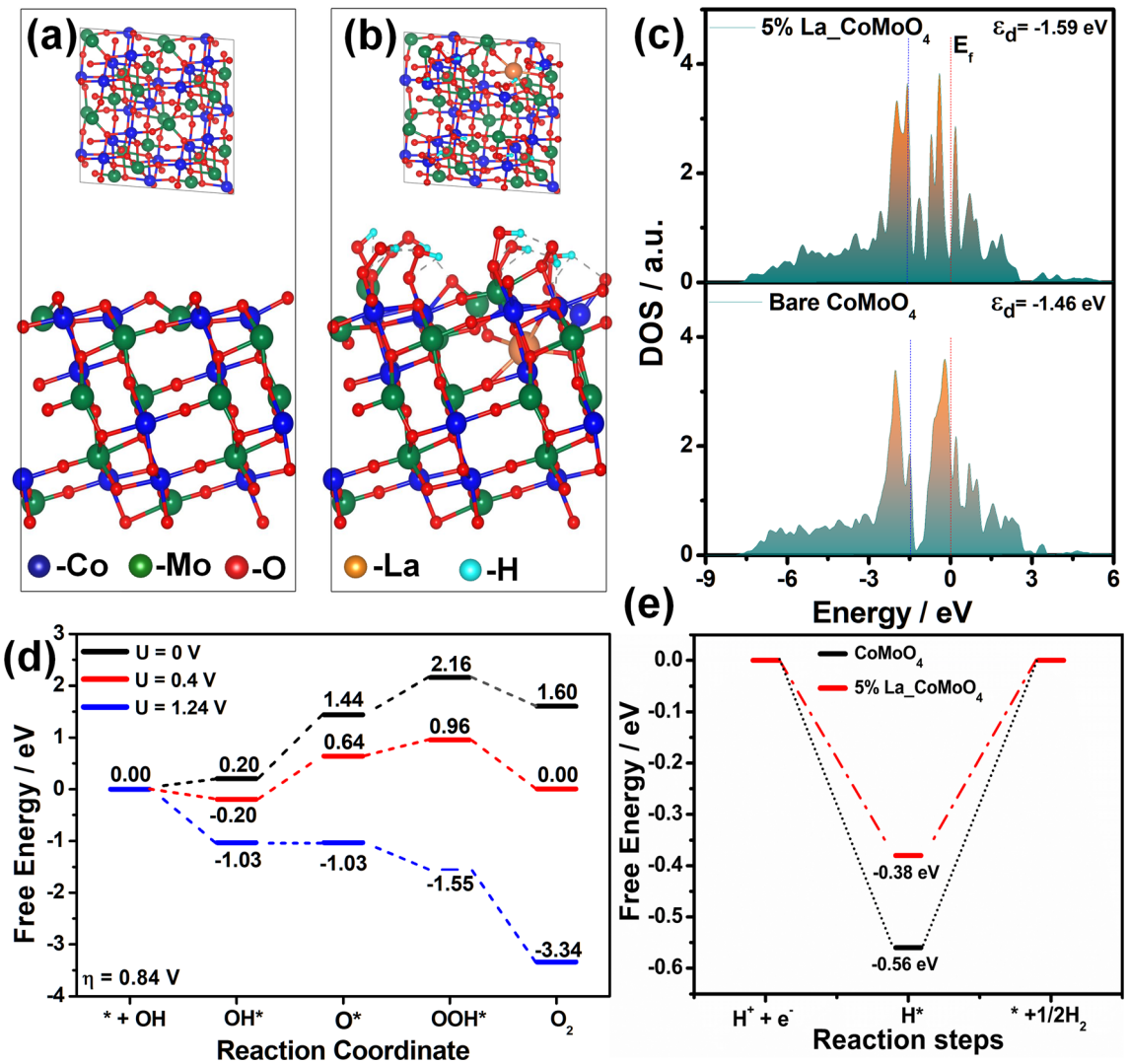

Fig. 9 DFT analysis of the 5% La_$CoMoO_4$ catalyst. Side and top views of the constructed supercell models of (a) bare $CoMoO_4$ and (b) OOH-covered La-doped $CoMoO_4$. Insets are the unit cell model of bare $CoMoO_4$ and La-doped $CoMoO_4$. The blue, green, red, orange, and cyan spheres represent Co, Mo, O, H, and La atoms, respectively. (c) The density of states of the Co atom in bare $CoMoO_4$ and 5% La_$CoMoO_4$. The dotted red line indicates the Fermi level, and the blue line indicates the d-band center. (d) Free energy plots of OER intermediates on the Co-site in the 5% La_$CoMoO_4$ system under different thermodynamic potentials in alkaline media. (e) Free energy plots of HER intermediates on the Mo-site of $CoMoO_4$ and La-doped $CoMoO_4$ in 5% La_$CoMoO_4$ system in alkaline media.

for doping (Fig. S16a and b ESI†). Then, the suitable site is found using the formation energy. The dopant formation energy is calculated using the formula,

$$E_F = E_{LaCoMoO_4} - E_{CoMoO_4} - nE_{La} + nE_{Co}$$

$E_{LaCoMoO_4}$ – total energy of La-doped $CoMoO_4$, E_{CoMoO_4} – total energy of pristine $CoMoO_4$, n – number of La atoms doped, E_{La} – total energy of La ad-atom, E_{Co} – total energy of Co ad-atom.

The La-dopant formation energy for the first layer is −1.26 eV and −3.95 eV for the second layer. The lower formation energy in the second layer shows that La doping is energetically favorable. On the La-doped $CoMoO_4$ surface, all the surface Co-atoms except one atom are covered with an OOH molecule (seven Co atoms, *i.e.*, 0.875 coverage). This is to simulate the experimental condition during the reaction, where the coordinatively unsaturated sites are saturated with OOH molecules, and for the pure $CoMoO_4$ case, where the OOH molecule dissociated.[72] In this case, the OER overpotential is drastically reduced to 0.84 V (Fig. 9d). To simplify, the potential required in addition to the OER equilibrium potential ($U = 0.4$ V) such that the process is spontaneous is the overpotential. Therefore, at the potential of $U = 1.24$ V (0.4 V + 0.84 V), the OER reaction proceeds for the La_$CoMoO_4$ case.

To further comprehend the electronic effects induced by La doping in $CoMoO_4$ and their influence on the electrocatalytic activity of 5% La_$CoMoO_4$, we performed the density of states (DOS) calculations, as shown in Fig. 9c. The d-band center of Co atoms before and after doping is analyzed to understand the catalytic activity. Accordingly, the d-band center of the Co atom in bare $CoMoO_4$ is closer to the Fermi level (−1.46 eV) compared to the 5% La_$CoMoO_4$ (−1.59 eV). Closer to the Fermi level indicates empty higher energy states, and therefore, stronger binding tendency of oxygen intermediates, resulting in higher O-atom binding and OOH dissociation. The downward shift of the d-band center after La doping leads to lower binding of the O-atom intermediate, thus lowering the overpotential. This is seen from the positive ΔG_O (0.64 eV) and ΔG_{OH} (0.96 eV) at the equilibrium potential. Thus, the introduction of La altered the electronic structure, potentially enhancing catalytic activity by modifying the electronic distribution around the Co centers. Furthermore, charge transfer is analyzed with Bader charge analysis, which was performed to quantify the charge transfer between pure $CoMoO_4$ and La-doped $CoMoO_4$. The charge on Co-atom in $CoMoO_4$ is +1.28|e| and that of 5% La_$CoMoO_4$ is +0.59|e| (positive sign indicates charge deficient). La dopant donates electrons to the nearby Co-atoms. This is also evident from the free energy, as O* formation is the potential determining step.

Theoretically, effective HER catalysts promote the rapid adsorption of hydrogen and facilitate its quick release. From a thermodynamic perspective, the ideal Gibbs free energy of adsorbed hydrogen atoms is expected to be very near zero. Consequently, we first used DFT simulations to assess the Gibbs free energy of intermediates associated with the chemically adsorbed H* on the catalyst surface. For HER, Mo sites are regarded as HER active sites.[73,74] Typically, the process of activating the H_2O molecule to reach the transition state (TS) is the phase that determines the rate of alkaline HER. The HER activity is usually determined by the Gibbs free energy of H adsorption (ΔG_{H^*}). According to Sabatier's principle, the closer the ΔG_{H^*} value of H_{ads} to the ideal value (0 eV) on the active site of a catalyst, the lower the energy barrier. Herein, the optimal loading of La (5%) should have a reasonable hydrogen binding energy (HBE) during the Heyrovsky step in an alkaline environment to regulate the adsorption of H* on the active Mo-sites and subsequent desorption of H_2. For $CoMoO_4$, ΔG_{H^*} of −0.56 eV indicates higher binding, thus poor HER activity, whereas for the 5% La_$CoMoO_4$, it is reduced to −0.38 eV (Fig. 9e). Thus, the reduced energy barrier for 5% La_$CoMoO_4$ infers superior HER performance after La doping in the $CoMoO_4$ lattice, optimizing ΔG_{H^*} towards the ideal value. Furthermore, the d-band center of the Mo atom in bare $CoMoO_4$ and 5% La_$CoMoO_4$ are computed to be −1.82 eV and −1.52 eV, respectively. The upward shift of the Mo d-band center toward E_F implies improved HER activity for 5% La_$CoMoO_4$ in line with electrochemical HER. Overall, the findings show that La doping improves the OER and HER catalytic activity of the $CoMoO_4$ catalyst.

4. Conclusions

In conclusion, a series of La-doped $CoMoO_4$ nanostructures of varying dopant percentages were synthesized by a simple one-step hydrothermal reaction. La doping in the $CoMoO_4$ lattice influences the electrocatalytic performance of $CoMoO_4$ toward HER and OER in 1 M KOH media by improving the conductivity and intrinsic activity of the catalyst. The optimal activity was achieved at 5% La_$CoMoO_4$ and showed spectacular durability under long-term electrochemical conditions while mitigating significant MoO_4^{2-} leaching in the electrolyte media. When assembled in a two-electrode water electrolyzer unit, 5% La_$CoMoO_4$‖5% La_$CoMoO_4$ (cathode and anode) delivered a cell potential of 1.68 V toward overall water splitting in 1 M KOH. DFT calculations illustrate a modulated electronic structure through La doping by downshifting the d-band center of Co atoms, thereby optimizing adsorption energies of reactive hydrogen and oxygen intermediates and boosting the intrinsic activity of $CoMoO_4$ toward OER and HER.

Data availability

Raw data supporting the study are available from the corresponding authors upon reasonable requests.

Author contributions

Bharathi Arumugam carried out the experimental work, fundamental characterizations, electrochemical studies, and original draft writing; Erakulan E. Siddharthan, and Ranjit Thapa, executed the DFT calculations and data analysis; Pandian Mannu and Chung-Li Dong executed *in situ* Raman and helped with post-catalysis characterization. Arokia Anto Jeffery and Seong-Cheol Kim designed and supervised the work and

edited the manuscript. All authors were involved in reviewing and finalizing the manuscript.

Conflicts of interest

There are no conflicts to declare.

Acknowledgements

The Basic Science Research Program supported this research through the National Research Foundation of Korea (NRF), funded by the Ministry of Education (2020R1I1A3052258). The authors (P. M. and C. L. D.) would like to thank the National Science and Technology Council of Taiwan (NSTC) under the contracts 113-2112-M-032-012.

References

1 J. H. Jang, A. A. Jeffery, J. Min, N. Jung and S. J. Yoo, Emerging Carbon Shell-Encapsulated Metal Nanocatalysts for Fuel Cells and Water Electrolysis, *Nanoscale*, 2021, **13**(36), 15116–15141, DOI: **10.1039/d1nr01328a**.

2 J. O. M. Bockris, The Origin of Ideas on a Hydrogen Economy and Its Solution to the Decay of the Environment, *Int. J. Hydrogen Energy*, 2002, **27**(7–8), 731–740, DOI: **10.1016/S0360-3199(01)00154-9**.

3 S. Kumar, R. Kaur and S. Sharma, Recent Reports on Hydrogen Evolution Reactions and Catalysis, *Results Chem.*, 2022, **4**, 100613, DOI: **10.1016/j.rechem.2022.100613**.

4 A. Raveendran, M. Chandran and R. Dhanusuraman, A Comprehensive Review on the Electrochemical Parameters and Recent Material Development of Electrochemical Water Splitting Electrocatalysts, *RSC Adv.*, 2023, **13**(6), 3843–3876, DOI: **10.1039/d2ra07642j**.

5 M. Zlatar, D. Escalera-López, M. G. Rodríguez, T. Hrbek, C. Götz, R. Mary Joy, A. Savan, H. P. Tran, H. N. Nong, P. Pobedinskas, V. Briega-Martos, A. Hutzler, T. Böhm, K. Haenen, A. Ludwig, I. Khalakhan, P. Strasser and S. Cherevko, Standardizing OER Electrocatalyst Benchmarking in Aqueous Electrolytes: Comprehensive Guidelines for Accelerated Stress Tests and Backing Electrodes, *ACS Catal.*, 2023, **13**(23), 15375–15392, DOI: **10.1021/acscatal.3c03880**.

6 J. Wang, X. Yue, Y. Yang, S. Sirisomboonchai, P. Wang, X. Ma, A. Abudula and G. Guan, Earth-Abundant Transition-Metal-Based Bifunctional Catalysts for Overall Electrochemical Water Splitting: A Review, *J. Alloys Compd.*, 2020, **819**, 153346, DOI: **10.1016/j.jallcom.2019.153346**.

7 M. I. Jamesh, D. Hu, J. Wang, F. Naz, J. Feng, L. Yu, Z. Cai, J. C. Colmenares, D. J. Lee, P. K. Chu and H. Y. Hsu, Recent Advances in Noble Metal-Free Electrocatalysts to Achieve Efficient Alkaline Water Splitting, *J. Mater. Chem. A*, 2024, 11771–11820, DOI: **10.1039/d3ta07418h**.

8 M. Yu, E. Budiyanto and H. Tüysüz, Principles of Water Electrolysis and Recent Progress in Cobalt-, Nickel-, and Iron-Based Oxides for the Oxygen Evolution Reaction, *Angew. Chem., Int. Ed.*, 2022, **61**(1), e202103824, DOI: **10.1002/anie.202103824**.

9 F. Qin, Z. Zhao, M. K. Alam, Y. Ni, F. Robles-Hernandez, L. Yu, S. Chen, Z. Ren, Z. Wang and J. Bao, Trimetallic NiFeMo for Overall Electrochemical Water Splitting with a Low Cell Voltage, *ACS Energy Lett.*, 2018, **3**(3), 546–554, DOI: **10.1021/acsenergylett.7b01335**.

10 K. Kawashima, C. L. Cao, H. Li, R. A. Márquez-Montes, B. R. Wygant, Y. J. Son, J. V. Guerrera, G. Henkelman and C. B. Mullins, Evaluation of a V8C7Anode for Oxygen Evolution in Alkaline Media: Unusual Morphological Behavior, *ACS Sustain. Chem. Eng.*, 2020, **8**(37), 14101–14108, DOI: **10.1021/acssuschemeng.0c04759**.

11 C. Liu, G. Bai, X. Tong, Y. Wang, B. Lv, N. Yang and X. Y. Guo, Mesoporous and Ultrathin Arrays of Cobalt Nitride Nanosheets for Electrocatalytic Oxygen Evolution, *Electrochem. Commun.*, 2019, **98**, 87–91, DOI: **10.1016/j.elecom.2018.11.022**.

12 J. Huang, Y. Jiang, T. An and M. Cao, Increasing the Active Sites and Intrinsic Activity of Transition Metal Chalcogenide Electrocatalysts for Enhanced Water Splitting, *J. Mater. Chem. A*, 2020, **8**(48), 25465–25498, DOI: **10.1039/d0ta08802a**.

13 A. A. Jeffery, J. Min, Y. Kim, S. S. Chougule, S. Lee, J. R. Jeong and N. Jung, PH-Induced Morphological Transformation of WxMoS2 Nanosheets for Hydrogen Evolution Reaction through Precursor Solution Aging, *J. Power Sources*, 2022, **526**, 231154, DOI: **10.1016/j.jpowsour.2022.231154**.

14 S. S. Chougule, B. Arumugam, J. K. Alagarasan, I. Hasan, N. Thomas, V. Rajashekar, R. Srinivasan, A. K. Yadav, P. Somu, M. Lee and A. A. Jeffery, Amorphous MoWSx Alloy Nanosheets via Room-Temperature Precipitation Method for Enhanced Electrocatalytic Hydrogen Evolution Reactions, *ACS Appl. Energy Mater.*, 2024, **7**(5), 1949–1960, DOI: **10.1021/acsaem.3c03098**.

15 P. M. Bodhankar, P. B. Sarawade, P. Kumar, A. Vinu, A. P. Kulkarni, C. D. Lokhande and D. S. Dhawale, Nanostructured Metal Phosphide Based Catalysts for Electrochemical Water Splitting: A Review, *Small*, 2022, **18**(21), 1–25, DOI: **10.1002/smll.202107572**.

16 A. Mariappan, R. K. Dharman and T. H. Oh, Metal-Organic Frameworks Derived FeS2@CoS2 Heterostructure for Efficient and Stable Bifunctional Electrocatalytic Water Splitting, *Ceram. Int.*, 2023, **49**(18), 29984–29990, DOI: **10.1016/j.ceramint.2023.06.255**.

17 R. K. Dharman, B. Mary Francis, J. S. Ponraj, S. C. Dhanabalan, R. K. Manavalan and T. H. Oh, Study on Nickel-Induced 1T/2H MoS2 Nanostructures in Realizing Efficient Electrocatalysts for Hydrogen Evolution Reaction, *J. Electroanal. Chem.*, 2022, **925**, 116905, DOI: **10.1016/j.jelechem.2022.116905**.

18 A. Mariappan, P. Mannu, K. S. Ranjith, T. T. T. Nga, Y. K. Han, C. L. Dong, R. K. Dharman and T. H. Oh, Novel Heterostructure-Based CoFe and Cobalt Oxysulfide Nanocubes for Effective Bifunctional Electrocatalytic Water and Urea Oxidation, *Small*, 2024, **2310112**, 1–11, DOI: **10.1002/smll.202310112**.

19 M. Yu, C. K. Chan and H. Tüysüz, Coffee-Waste Templating of Metal Ion-Substituted Cobalt Oxides for the Oxygen Evolution Reaction, *ChemSusChem*, 2018, **11**(3), 605–611, DOI: **10.1002/cssc.201701877**.

20 A. A. Jeffery, S. S. Chougule, I. Hasan, J. K. Alagarasan, P. Ravi Sankar, P. Somu, M. C. Lin, K. Kumarasamy, Y. H. Ahn and J. Murugasamy, Oxygen-Vacancy-Rich HfO2-x Nanoparticles Supported on Reduced Graphene Oxide for Electrocatalytic Hydrogen Evolution Reactions, *ACS Appl. Nano Mater.*, 2023, **6**(24), 23053–23063, DOI: **10.1021/acsanm.3c04439**.

21 M. S. Burke, M. G. Kast, L. Trotochaud, A. M. Smith and S. W. Boettcher, Cobalt-Iron (Oxy)Hydroxide Oxygen Evolution Electrocatalysts: The Role of Structure and Composition on Activity, Stability, and Mechanism, *J. Am. Chem. Soc.*, 2015, **137**(10), 3638–3648, DOI: **10.1021/jacs.5b00281**.

22 S. Verma, S. Sinha-Ray and S. Sinha-Ray, Electrospun CNF Supported Ceramics as Electrochemical Catalysts for Water Splitting and Fuel Cell: A Review, *Polymers*, 2020, **12**(1), 43–47, DOI: **10.3390/POLYM12010238**.

23 M. Safdar, M. Iftikhar, S. Rashid, M. Awais, A. Iqbal, A. Bilal, S. Aslam and M. Mirza, Synthesis and Investigation of Catalytic HER/OER Performances of Al2SSe in Alkaline/Acidic Media and Water Detoxification Behavior, *Int. J. Hydrogen Energy*, 2024, **50**, 107–117, DOI: **10.1016/j.ijhydene.2023.07.252**.

24 J. M. Gonçalves, P. R. Martins, K. Araki and L. Angnes, Recent Progress in Water Splitting and Hybrid Supercapacitors Based on Nickel-Vanadium Layered Double Hydroxides, *J. Energy Chem.*, 2021, **57**, 496–515, DOI: **10.1016/j.jechem.2020.08.047**.

25 R. Nadarajan, A. V. Gopinathan, N. P. Dileep, A. S. Sidharthan and M. M. Shaijumon, Heterointerface Engineering of Cobalt Molybdenum Suboxide for Overall Water Splitting, *Nanoscale*, 2023, **15**(37), 15219–15229, DOI: **10.1039/d3nr02458j**.

26 X. Wang, G. She, L. Mu and W. Shi, Amorphous Co-Mo-P-O Bifunctional Electrocatalyst via Facile Electrodeposition for Overall Water Splitting, *ACS Sustain. Chem. Eng.*, 2020, **8**(7), 2835–2842, DOI: **10.1021/acssuschemeng.9b06929**.

27 J. Gautam, D. Chanda, M. Mekete Meshesha, S. G. Jang and B. Lyong Yang, Manganese Cobalt Sulfide/Molybdenum Disulfide Nanowire Heterojunction as an Excellent Bifunctional Catalyst for Electrochemical Water Splitting, *J. Colloid Interface Sci.*, 2023, **638**, 658–671, DOI: **10.1016/j.jcis.2023.02.029**.

28 X. Du, G. Ma and X. Zhang, Mo-Doped Co9S8 Nanorod Array as a High Performance Electrochemical Water Splitting Catalyst in Alkaline Solution, *Int. J. Hydrogen Energy*, 2019, **44**(51), 27765–27771, DOI: **10.1016/j.ijhydene.2019.09.003**.

29 J. Wang, J. Hu, C. Liang, L. Chang, Y. Du, X. Han, J. Sun and P. Xu, Surface Reconstruction of Phosphorus-Doped Cobalt Molybdate Microarrays in Electrochemical Water Splitting, *Chem. Eng. J.*, 2022, **446**(P3), 137094, DOI: **10.1016/j.cej.2022.137094**.

30 L. Ge, W. Lai, Y. Deng, J. Bao, B. Ouyang and H. Li, Spontaneous Dissolution of Oxometalates Boosting the Surface Reconstruction of CoMOx(M = Mo, V) to Achieve Efficient Overall Water Splitting in Alkaline Media, *Inorg. Chem.*, 2022, **61**(5), 2619–2627, DOI: **10.1021/acs.inorgchem.1c03677**.

31 S. Chamani, E. Sadeghi, U. Unal, N. S. Peighambardoust and U. Aydemir, Tuning Electrochemical Hydrogen-Evolution Activity of $CoMoO_4$ through Zn Incorporation, *Catalysts*, 2023, **13**(5), 798, DOI: **10.3390/catal13050798**.

32 C. T. Moi, A. Sahu and M. Qureshi, Tapping the Potential of High-Valent Mo and W Metal Centers for Dynamic Electronic Structures in Multimetallic FeVO(OH)/$Ni(OH)_2$ for Ultrastable and Efficient Overall Water Splitting, *ACS Appl. Mater. Interfaces*, 2023, **15**, 5336–5344, DOI: **10.1021/acsami.2c21041**.

33 Y. Liu, P. Xu, Z. Ye, T. Cen, X. Peng, D. Yuan and H. P. Wu, Doped CoMoO4/RGO as an Efficient Hybrid Catalyst for Hydrogen Evolution, *Int. J. Hydrogen Energy*, 2020, **45**(30), 15157–15165, DOI: **10.1016/j.ijhydene.2020.04.008**.

34 H. Sun, X. Xu, H. Kim, W. C. Jung, W. Zhou and Z. Shao, Electrochemical Water Splitting: Bridging the Gaps Between Fundamental Research and Industrial Applications, *Energy Environ. Mater.*, 2023, **6**(5), 1–21, DOI: **10.1002/eem2.12441**.

35 L. Xiao, Y. Wang, T. Fu, Q. Liu, F. Guo, Y. Zhang, M. Li, X. Bo and T. Liu, Facile Synthesis of Ultrafine Iron-Cobalt (FeCo) Nanocrystallite-Embedded Boron/Nitrogen-Codoped Porous Carbon Nanosheets: Accelerated Water Splitting Catalysts, *J. Colloid Interface Sci.*, 2024, **654**(PA), 150–163, DOI: **10.1016/j.jcis.2023.10.026**.

36 R. Wu, J. Xu, C. L. Zhao, X. Z. Su, X. L. Zhang, Y. R. Zheng, F. Y. Yang, X. S. Zheng, J. F. Zhu, J. Luo, W. X. Li, M. R. Gao and S. H. Yu, Dopant Triggered Atomic Configuration Activates Water Splitting to Hydrogen, *Nat. Commun.*, 2023, **14**(1), 2306, DOI: **10.1038/s41467-023-37641-3**.

37 D. Rathore, S. Ghosh, J. Chowdhury and S. Pande, Fe-Doped NiCo 2 Se 4 Nanorod Arrays as Electrocatalysts for Overall Electrochemical Water Splitting, *ACS Appl. Nano Mater.*, 2023, **6**(4), 3095–3110, DOI: **10.1021/acsanm.3c00265**.

38 W. S. Lin, M. Rinawati, W. H. Huang, C. Y. Chang, L. Y. Chang, Y. S. Cheng, C. C. Chang, J. L. Chen, W. N. Su and M. H. Yeh, Surface Restructuring Prussian Blue Analog-Derived Bimetallic CoFe Phosphides by N-Doped Graphene Quantum Dots for Electroactive Hydrogen Evolving Catalyst, *J. Colloid Interface Sci.*, 2024, **654**(PA), 677–687, DOI: **10.1016/j.jcis.2023.10.028**.

39 F. T. Dajan, M. G. Sendeku, B. Wu, N. Gao, E. F. Anley, J. Tai, X. Zhan, Z. Wang, F. Wang and J. He, Ce Site in Amorphous Iron Oxyhydroxide Nanosheet toward Enhanced Electrochemical Water Oxidation, *Small*, 2023, **19**(27), 1–8, DOI: **10.1002/smll.202207999**.

40 P. Wei, X. Li, Z. He, Z. Li, X. Zhang, X. Sun, Q. Li, H. Yang, J. Han and Y. Huang, Electron Density Modulation of MoP by Rare Earth Metal as Highly Efficient Electrocatalysts for PH-Universal Hydrogen Evolution Reaction, *Appl. Catal., B*, 2021, **299**, 120657, DOI: **10.1016/j.apcatb.2021.120657**.

41 Z. Wan, M. Hu, B. Hu, T. Yan, K. Wang and X. Wang, Vacancy Induced Photocatalytic Activity of La Doped In(OH)3 for CO2 Reduction with Water Vapor, *Catal. Sci. Technol.*, 2020, **10**(9), 2893–2904, DOI: **10.1039/d0cy00029a**.

42 N. S. Gultom, Y. C. Zhou and D. H. Kuo, A Facile and Efficient Method for Preparing La-Doped Co3O4 by Electrodeposition as an Efficient Air Cathode in Rechargeable Zinc-Air Batteries: Role of Oxygen Vacancies, *J. Colloid Interface Sci.*, 2024, **655**(43), 394–406, DOI: **10.1016/j.jcis.2023.11.021**.

43 H. Sudrajat, M. Kitta, R. Ito, S. Nagai, T. Yoshida, R. Katoh, B. Ohtani, N. Ichikuni and H. Onishi, Water-Splitting Activity of La-Doped NaTaO3Photocatalysts Sensitive to Spatial Distribution of Dopants, *J. Phys. Chem. C*, 2020, **124**(28), 15285–15294, DOI: **10.1021/acs.jpcc.0c03822**.

44 K. Eda, Y. Uno, N. Nagai, N. Sotani and M. S. Whittingham, Crystal Structure of Cobalt Molybdate Hydrate CoMoO4·NH2O, *J. Solid State Chem.*, 2005, **178**(9), 2791–2797, DOI: **10.1016/j.jssc.2005.06.014**.

45 A. Karmakar and S. Kundu, A Concise Perspective on the Effect of Interpreting the Double Layer Capacitance Data over the Intrinsic Evaluation Parameters in Oxygen Evolution Reaction, *Mater. Today Energy*, 2023, **33**, 101259, DOI: **10.1016/j.mtener.2023.101259**.

46 C. C. L. McCrory, S. Jung, J. C. Peters and T. F. Jaramillo, Benchmarking Heterogeneous Electrocatalysts for the Oxygen Evolution Reaction, *J. Am. Chem. Soc.*, 2013, **135**(45), 16977–16987, DOI: **10.1021/ja407115p**.

47 Z. Wang, Y. Chen, D. Zeng, Q. Zhang and D. L. Peng, Solution Synthesis of Triangular and Hexagonal Nickel Nanosheets with the Aid of Tungsten Hexacarbonyl, *CrystEngComm*, 2016, **18**(8), 1295–1301, DOI: **10.1039/c5ce02187a**.

48 W. Wang and J. Xu, Structure and Visible Light Luminescence of 3D Flower-like Co3O4 Hierarchical Microstructures Assembled by Hexagonal Porous Nanoplates, *ACS Appl. Mater. Interfaces*, 2015, **7**(1), 415–421, DOI: **10.1021/am506414n**.

49 Z. Xiao, W. Zhou, B. Yang, C. Liao, Q. Kang, G. Chen, M. Liu, X. Liu, R. Ma and N. Zhang, Tuned D-Band States over Lanthanum Doped Nickel Oxide for Efficient Oxygen Evolution Reaction, *Nano Mater. Sci.*, 2023, **5**(2), 228–236, DOI: **10.1016/j.nanoms.2022.07.002**.

50 H. Kabir, S. H. Nandyala, M. M. Rahman, M. A. Kabir and A. Stamboulis, Influence of Calcination on the Sol–Gel Synthesis of Lanthanum Oxide Nanoparticles, *Appl. Phys. A:Mater. Sci. Process.*, 2018, **124**(12), 1–11, DOI: **10.1007/s00339-018-2246-5**.

51 E. Sadeghi, S. Chamani, E. Erdem, N. S. Peighambardoust and U. Aydemir, NiMo/CoMoO4 Heterostructure with Confined Oxygen Vacancy for Active and Durable Alkaline Hydrogen Evolution Reaction, *ACS Appl. Energy Mater.*, 2023, **6**(14), 7658–7671, DOI: **10.1021/acsaem.3c01146**.

52 P. Wei, X. Li, Z. He, Z. Li, X. Zhang, X. Sun, Q. Li, H. Yang, J. Han and Y. Huang, Electron Density Modulation of MoP by Rare Earth Metal as Highly Efficient Electrocatalysts for PH-Universal Hydrogen Evolution Reaction, *Appl. Catal., B*, 2021, **299**(0926–3373), 120657, DOI: **10.1016/j.apcatb.2021.120657**.

53 X. Du, J. Huang, J. Zhang, Y. Yan, C. Wu, Y. Hu, C. Yan, T. Lei, W. Chen, C. Fan and J. Xiong, Modulating Electronic Structures of Inorganic Nanomaterials for Efficient Electrocatalytic Water Splitting, *Angew. Chem., Int. Ed.*, 2019, **58**, 4484–4502, DOI: **10.1002/anie.201810104**.

54 S. Anantharaj, S. Noda, M. Driess and P. W. Menezes, The Pitfalls of Using Potentiodynamic Polarization Curves for Tafel Analysis in Electrocatalytic Water Splitting, *ACS Energy Lett.*, 2021, **6**(4), 1607–1611, DOI: **10.1021/acsenergylett.1c00608**.

55 H. N. Dhandapani, R. Madhu, A. De, M. A. Salem, B. Ramesh Babu and S. Kundu, Tuning the Surface Electronic Structure of Amorphous NiWO4 by Doping Fe as an Electrocatalyst for OER, *Inorg. Chem.*, 2023, **62**(30), 11817–11828, DOI: **10.1021/acs.inorgchem.3c01095**.

56 S. Singha Roy, A. Karmakar, R. Madhu, S. Nagappan, H. N Dhandapani and S. Kundu, Three-Dimensional Sm-Doped NiCu-LDH on Ni Foam as a Highly Robust Bifunctional Electrocatalyst for Total Water Splitting, *ACS Appl. Energy Mater.*, 2023, **6**(17), 8818–8829, DOI: **10.1021/acsaem.3c01338**.

57 Y. Zhang, H. Guo, P. Yuan, K. Pang, B. Cao, X. Wu, L. Zheng and R. Song, Structural Evolution of CoMoO4 to CoOOH by Ion Electrochemical Etching for Boosting Oxygen Evolution Reaction, *J. Power Sources*, 2019, **442**, 227252, DOI: **10.1016/j.jpowsour.2019.227252**.

58 R. N. Dürr, P. Maltoni, H. Tian, B. Jousselme, L. Hammarström and T. Edvinsson, From NiMoO4to γ-NiOOH: Detecting the Active Catalyst Phase by Time Resolved in Situ and Operando Raman Spectroscopy, *ACS Nano*, 2021, **15**(8), 13504–13515, DOI: **10.1021/acsnano.1c04126**.

59 A. Rajput, M. K. Adak and B. Chakraborty, Intrinsic Lability of NiMoO4to Excel the Oxygen Evolution Reaction, *Inorg. Chem.*, 2022, **61**(29), 11189–11206, DOI: **10.1021/acs.inorgchem.2c01167**.

60 H. Yin, H. Xiao, R. Qin, J. Chen, F. Tan, W. Zhang, J. Zhao, L. Zeng, Y. Hu, F. Pan, P. Lei, S. Yuan, L. Qian, Y. Su and Z. Zhang, Lattice Strain Mediated Reversible Reconstruction in CoMoO4·0.69H2O for Intermittent Oxygen Evolution, *ACS Appl. Mater. Interfaces*, 2023, **15**(16), 20100–20109, DOI: **10.1021/acsami.3c00544**.

61 J. Wang, J. Hu, C. Liang, L. Chang, Y. Du, X. Han, J. Sun and P. Xu, Surface Reconstruction of Phosphorus-Doped Cobalt Molybdate Microarrays in Electrochemical Water Splitting, *Chem. Eng. J.*, 2022, **446**(3), 137094, DOI: **10.1016/j.cej.2022.137094**.

62 J. Sun, G. Ren, S. Qin, Z. Zhao, Z. Li, Z. Zhang, C. Li and X. Meng, Reconstruction Co-O-Mo in Amorphous-Crystalline MoOx/Co(OH)2 Interface for Industry-Level Active and Stable Electrocatalytic Seawater Hydrogen Evolution, *Nano Energy*, 2024, **121**, 109246, DOI: **10.1016/j.nanoen.2023.109246**.

63 F. Wang, L. Hu, R. Deng, S. Dai, D. Lu, X. Chen, X. Pan, X. Ren, D. Dong, R. Weng, G. Xu and H. Yang, Regulation

of Bulk Reconstruction of FeNiMoO4via NH3 Treatment for High Performance Water Oxidation, *Inorg. Chem. Front.*, 2023, **10**(12), 3621–3631, DOI: 10.1039/d3qi00461a.

64 Z. Liu, K. Wang, X. Tong, F. Kong and Y. Cao, Deep Reconstruction of Fe-NiMoO4·nH2O@NiOOH as Efficient Oxygen Evolution Electrocatalysts, *Energy Fuels*, 2023, **37**(4), 3023–3030, DOI: 10.1021/acs.energyfuels.2c03732.

65 Y. Wang, B. Wang, F. Xiao, Z. Huang, Y. Wang, C. Richardson, Z. Chen, L. Jiao and H. Yuan, Facile Synthesis of Nanocage Co3O4 for Advanced Lithium-Ion Batteries, *J. Power Sources*, 2015, **298**, 203–208, DOI: 10.1016/j.jpowsour.2015.07.014.

66 A. Moysiadou, S. Lee, C. S. Hsu, H. M. Chen and X. Hu, Mechanism of Oxygen Evolution Catalyzed by Cobalt Oxyhydroxide: Cobalt Superoxide Species as a Key Intermediate and Dioxygen Release as a Rate-Determining Step, *J. Am. Chem. Soc.*, 2020, **142**(27), 11901–11914, DOI: 10.1021/jacs.0c04867.

67 R. N. Dürr, P. Maltoni, H. Tian, B. Jousselme, L. Hammarström and T. Edvinsson, From NiMoO4 to γ-NiOOH: Detecting the Active Catalyst Phase by Time Resolved in Situ and Operando Raman Spectroscopy, *ACS Nano*, 2021, **15**(8), 13504–13515, DOI: 10.1021/acsnano.1c04126.

68 S. Yang, L. Lu, P. Zhan, Z. Si, L. Chen, Y. Zhuang and P. Qin, Amorphous Hetero-Structure Iron/Cobalt Oxyhydroxide with Atomic Dispersed Palladium for Oxygen Evolution Reaction, *Appl. Catal., B*, 2024, **355**(0926–3373), 124213, DOI: 10.1016/j.apcatb.2024.124213.

69 F. Wang, L. Hu, R. Deng, S. Dai, D. Lu, X. Chen, X. Pan, X. Ren, D. Dong, R. Weng, G. Xu and H. Yang, Regulation of Bulk Reconstruction of FeNiMoO4via NH3 Treatment for High Performance Water Oxidation, *Inorg. Chem. Front.*, 2023, **10**(12), 3621–3631, DOI: 10.1039/d3qi00461a.

70 X. Zhang, H. Zhong, Q. Zhang, Q. Zhang, C. Wu, J. Yu, Y. Ma, H. An, H. Wang, Y. Zou, C. Diao, J. Chen, Z. G. Yu, S. Xi, X. Wang and J. Xue, High-Spin Co3+ in Cobalt Oxyhydroxide for Efficient Water Oxidation, *Nat. Commun.*, 2024, **15**(1), 1–10, DOI: 10.1038/s41467-024-45702-4.

71 J. K. Nørskov, J. Rossmeisl, A. Logadottir, L. Lindqvist, J. R. Kitchin, T. Bligaard and H. Jónsson, Origin of the Overpotential for Oxygen Reduction at a Fuel-Cell Cathode, *J. Phys. Chem. B*, 2004, **108**(46), 17886–17892, DOI: 10.1021/jp047349j.

72 P. Bhol, S. A. Patil, N. Barman, E. E. Siddharthan, R. Thapa, M. Saxena, A. Altaee and A. K. Samal, Design and Fabrication of Cobaltx Nickel(1-x) Telluride Microfibers on Nickel Foam for Battery-Type Supercapacitor and Oxygen Evolution Reaction Study, *Mater. Today Chem.*, 2023, **30**, 101557, DOI: 10.1016/j.mtchem.2023.101557.

73 Z. Wang, M. T. Tang, A. Cao, K. Chan and J. K. Norskov, Insights into the Hydrogen Evolution Reaction on 2D Transition-Metal Dichalcogenides, *J. Phys. Chem. C*, 2022, **126**(11), 5151–5158, DOI: 10.1021/acs.jpcc.1c10436.

74 L. Jiang, Y. J. Zhang, X. H. Luo, L. Yu, H. X. Li and Y. J. Li, Se and O Co-Insertion Induce the Transition of MoS2 from 2H to 1T Phase for Designing High-Active Electrocatalyst of Hydrogen Evolution Reaction, *Chem. Eng. J.*, 2021, **425**, 1–9, DOI: 10.1016/j.cej.2021.130611.